

PHOTOCATALYSIS OF CERIUM-ZIRCONIUM DIOXIDE SOLID SOLUTION
NANOPARTICLE FREE RADICAL SCAVENGERS

By

RUI QING

A THESIS PRESENTED TO THE GRADUATE SCHOOL
OF THE UNIVERSITY OF FLORIDA IN PARTIAL FULFILLMENT
OF THE REQUIREMENTS FOR THE DEGREE OF
MASTER OF SCIENCE

UNIVERSITY OF FLORIDA

2009

© 2009 Rui Qing

ACKNOWLEDGMENTS

There are many people to thank for. Without their crucial support and help, I would not be able to complete this work and finish my master's degree.

First of all, I would like thank Dr. Wolfgang Sigmund for his compassion, inspiration, consideration and guidance towards this work. The enthusiasm, devotion, and philosophy he delivered to students are the key elements lead to the completion of this research. His mentoring and knowledge helped me in every aspect in accomplishing the goal of the project. I also like to thank my committee member, Dr. Dempere and Dr. Baney for their help all through my master's career. They are great examples for my development in the future.

I would also like to thank current and previous students in Dr. Sigmund's Group. They have helped me not only in sparking my interests and insights into the academic research, but also accompanying my life in the University of Florida. I thank Dr. Yi-Yang Tsai and Dr. Georgios Pyrgiotakis, who helped me a lot in building the system and discussing the results. I would give a warm thanks to Shu-Hau Hsu, Yi-Chung Wang, Karron Woan, Hyoungjun Park, Raymond Scheffler, Dr. Joshua Taylor and Michael Laudenslager, who have shared the precious memories with me here.

I would like to recognize the help of the staff, i.e. Ms. Kerry Siebein, Mr. Eric Lambers in MAIC (Major Analytical Instrumentation Center) and Gill Brubaker PERC (Particle Engineering Research Center) for their help in training me using the equipments and characterizing my samples.

Finally I would like to acknowledge my mother for her financial as well as mental support all through my life in the US. I also owe sincere thanks for all my friends who have been supportive in my life.

TABLE OF CONTENTS

	<u>page</u>
ACKNOWLEDGMENTS	3
LIST OF TABLES	6
LIST OF FIGURES	7
ABSTRACT.....	9
CHAPTER	
1 INTRODUCTION	10
1.1 Introduction.....	10
1.2 Motivation.....	11
1.3 Objective.....	11
2 BACKGROUND	13
2.1 Pshotocatalytic Materials.....	13
2.1.1 Basics of Semiconductor Photocatalysts	13
2.1.2 Nanosize Impact on Semiconductor Photocatalysts.....	15
2.2 Ceria and Cerium-Zirconium Dioxide Solid Solutions	17
2.2.1 CeO ₂ Nanoparticles in Biomedical Field	17
2.2.2 Cerium-Zirconium Solid Solutions	18
2.3 Cerium-Zirconium Solid Solution Application in Free Radical Scavenging	19
3 SYNTHESIS OF CERIUM-ZIRCONIUM DIOXIDE NANOPARTICLES.....	23
3.1 Reverse Micelle Method Synthesis	23
3.2 Synthesis of Ce _x Zr _{1-x} O ₂ Nanoparticles	24
3.3 Particle Dispersion.....	25
4 CHARACTERIZATION OF CERIUM-ZIRCONIUM DIOXIDE NANOPARTICLES.....	29
4.1 Chemical Ratio Determination	29
4.1.1 Inductively Couple Plasma Spectrometry (ICP)	29
4.1.2 Compositional Results.....	30
4.2 Particle Size Analysis	31
4.2.1 Dynamic Light Scattering Method	31
4.2.2 Size and Size Distribution of Ce _x Zr _{1-x} O ₂ nanoparticles	32
4.3 Structural Characterization by TEM.....	33
4.3.1 High-Resolution Transmission Electron Microscopy	33
4.3.2 TEM Results and Discussion.....	34

4.4	Structural Characterization by XPS.....	35
4.4.1	X-Ray Photoelectron Spectroscopy.....	35
4.4.2	Experimental.....	36
4.4.3	Results and Discussion.....	36
4.5	Electronic Properties Characterization by UV/Visible Spectroscopy.....	37
4.5.1	Absorption Spectrum by UV/Visible Spectroscopy.....	37
4.5.2	Tauc Relation and Bandgap Calculation.....	38
5	PHOTOCATALYSIS BY CERIUM-ZIRCONIUM DIOXIDE NANOPARTICLES.....	48
5.1	Experimental Setup and Procedures.....	48
5.1.1	Reactor Chamber Setup.....	48
5.1.2	Dye Selection.....	49
5.1.3	Procedures.....	49
5.2	Theory for Photocatalytic Degradation Reaction.....	50
5.3	Results and Discussion.....	52
5.3.1	Photocatalysis of $Ce_xZr_{1-x}O_2$ nanoparticles under 302 nm UV irradiation.....	52
5.3.2	Photocatalysis of $Ce_xZr_{1-x}O_2$ nanoparticles under 365 nm UV irradiation.....	53
5.3.3	Rate Constant Calculation and Implications.....	54
5.4	Summary.....	55
6	IMPLICATIONS AND CONCLUSIONS.....	61
6.1	Implications and Future Work.....	61
6.2	Conclusions.....	62
	LIST OF REFERENCES.....	64
	BIOGRAPHICAL SKETCH.....	70

LIST OF TABLES

<u>Table</u>		<u>page</u>
4-1	Cerium/Zirconium ratio for synthesized $Ce_xZr_{1-x}O_2$ nanoparticles by inductively coupled plasma.....	40
4-2	Size and specific surface area of $Ce_xZr_{1-x}O_2$ nanoparticles by dynamic light scattering method.....	40
4-3	XPS data for CeO_2 and $Ce_{0.4}Zr_{0.6}O_2$ nanoparticles.....	40
4-4	The calculated bandgap for direct band transition of $Ce_xZr_{1-x}O_2$ nanoparticles.....	41
5-1	Photocatalytic reaction intermediates summarized for different stages.....	57
5-2	Normalized rate constants of photocatalytic degradation of Procion Red MX-5B for the synthesized $Ce_xZr_{1-x}O_2$ nanoparticles under 302 nm and 365 nm UV illumination.....	57

LIST OF FIGURES

<u>Figure</u>	<u>page</u>
2-1 Schematic representation of the reactions taking place in a semiconductor photocatalyst	21
2-2 Schematic diagram showing the potentials for various redox processes occurring on the TiO ₂ surface at pH 7.....	21
2-3 Schematic graph of CeO ₂ fluorite structure	21
2-4 Phase diagram of Ce _x Zr _{1-x} O ₂ system.....	21
2-5 Reduction percentages of the Ce _x Zr _{1-x} O ₂ solid solutions as a function of reduction temperature	22
2-6 Rate constant for superoxide radical scavenging by Ce _x Zr _{1-x} O ₂ nanoparticles.....	22
3-1 Schematic view of reverse micelle method	26
3-2 Overall procedure of Ce _x Zr _{1-x} O ₂ nanoparticles synthesis.....	27
3-3 Optical image: Ce _x Zr _{1-x} O ₂ suspensions in different solvents	28
4-1 Constructive and destructive effect of light scattering	42
4-2 Size and distribution of Ce _x Zr _{1-x} O ₂ nanoparticles by dynamic light scattering method	43
4-3 TEM image of CeO ₂ nanoparticles.....	44
4-4 TEM image of Ce _{0.6} Zr _{0.4} O ₂ nanoparticles	45
4-5 TEM image of ZrO ₂ particles	46
4-6 UV/VIS absorption spectra for synthesized Ce _x Zr _{1-x} O ₂ nanoparticles.....	47
4-7 Fitting curve for direct band transition of ceria nanoparticles.....	47
5-1 Sketch of the reactor chamber	58
5-2 The chemical structure of Procion® Red MX-5B.....	58
5-3 The absorption spectrum for 5 ppm solution of the Procion® Red MX-5B dye	59
5-4 Time dependence of normalized residual dye concentration for irradiation with 302 nm UV light	59

5-5	Time dependence of normalized residual dye concentration for irradiation with 365 nm UV light	60
6-1	Schematic structure for CeO ₂ and Ce _x Zr _{1-x} O ₂ crystals.....	63
6-2	The reaction pathway for Ce _x Zr _{1-x} O ₂ nanoparticles free radical scavengers.....	63

Abstract of Thesis Presented to the Graduate School
of the University of Florida in Partial Fulfillment of the
Requirements for the Degree of Master of Science

PHOTOCATALYSIS OF CERIUM-ZIRCONIUM DIOXIDE SOLID SOLUTION
NANOPARTICLE FREE RADICAL SCAVENGERS

By

Rui Qing

May 2009

Chair: Wolfgang M. Sigmund
Major: Materials Science and Engineering

Free radical scavenging nanoparticles are based on semiconductors. In principal they should also be photo-catalytically active since they have a band gap. This work aimed to verify the level of photocatalytic activity for a series of $Ce_xZr_{1-x}O_2$ nanoparticles which were amongst the best free radical scavenging particles to date, even surpassing the activity of commercialized enzymes. The nanoparticles were synthesized by the reverse micelle method and characterized with various techniques.

The photocatalytic activity was determined by the degradation of Procion® Red MX-5B dye and compared to a commercially available photocatalyst, i.e. Aeroxide® TiO₂ P25 under UV light illumination with different wavelengths. It was found that free radical scavengers have the ability to act as free radical generators under UV-light, but the photocatalytic reaction constants were found to be one to two orders of magnitude lower than Aeroxide® TiO₂ P25 for dye degradation with 302 nm UV irradiation. No measureable reaction was observed for longer wavelengths. This suggests that the generation of free radicals by exposure of free radical scavenging particles under sunlight should be insignificant.

CHAPTER 1 INTRODUCTION

1.1 Introduction

Traditionally used for their mechanical property as ceramic polishing materials and glass sensitizers, ceria [cerium (IV) dioxide, CeO_2] are now being exploited extensively for its electronic properties in various applications. The unique capability of cerium atom to switch between Ce^{3+} and Ce^{4+} ionic state in oxidized and reduced condition enables it to be used widely in various catalytic and functional systems. Examples include histochemistry [1], three-way catalytic converters [2], electrolytes in solid oxide fuel cells [3, 4], gas sensors [5], oxygen storage materials [6] and water decomposition catalysts [7].

From the last decade, researchers started to relate many human disorders and malfunctions to the detrimental effect caused by reactive oxygen species (ROS) [8, 9]. The accreting impact of ROS could lead to the damage of living cells, and finally cause various kinds of human diseases, such as cancers, obesity, cardiovascular dysfunction, Parkinson's disease, etc..

Based on the non-biological applications of ceria-based materials, scientists tested them also in vivo systems utilizing their oxygen exchange properties. Potentially a panacea for harmful reactive oxygen species limiting the lifespan of living cells, ceria was investigated by many groups regarding these applications [8, 9]. Y.Y Tsai et al. had successfully established a reverse micelle method to synthesize nanosize ceria particles. They also tested the particles' capability in scavenging detrimental intracellular free radicals in vivo [8, 9]. Similar works also include Das et al.'s research in ceria's protective effect to spinal cord neurons [8, 9].

However, the performance of pure ceria in such applications was limited by its oxygen change capability involved in the process. Their overall activity was constrained by the equilibrium ratio between Ce^{3+} and Ce^{4+} in ceria materials. In 1950, Duwez and Odell

established the first phase diagram of cerium-zirconium dioxide quasi-binary system [10]. Proved to be effective in catalytic applications [11, 12], cerium-zirconium dioxide solid solution nanoparticles were now studied and reported to be an effective reactive oxygen species scavenger [13]. It was demonstrated by Y.Y. Tsai et al. that cerium-zirconium dioxide solid solution nanoparticles are effective in scavenging peroxide and superoxide free radicals. Even compared to the current commercialized enzyme scavenger SOD (Superoxide Dismutase), $Ce_xZr_{1-x}O_2$ nanoparticles had displayed a higher activity under similar conditions.

1.2 Motivation

This research focuses on a new aspect of these solid solution nanoparticles. Though widely acknowledged as a potential candidate for bio-protections, ceria and its solid solution with zirconia are still semiconductors. Such compounds are expected to behave as semiconductor photocatalysts when irradiated with light with photonic energy higher than their bandgap. Therefore, $Ce_xZr_{1-x}O_2$ should generate free radical species when exposed to UV light. To date there is no publication showing the magnitude of their photocatalytic activity. Furthermore, the quantum confinement in small particles additionally alters the band structure. This means that experimental data are of importance to allow calculation of bandgap and photocatalytic reaction constants. The ability for $Ce_xZr_{1-x}O_2$ nanoparticles to perform these reactions potentially hinders its application in free radical scavenging systems. Actually, it has been demonstrated that cerium dioxide is a potential photocatalyst that can be used to decompose water to produce oxygen in aqueous system with electron acceptors, i.e. Ce^{4+} or Fe^{3+} [7].

1.3 Objective

As has been mentioned above, CeO_2 is an excellent free radical scavenger when used in extending the lifespan of living cells in vivo. Thus there is huge potential that they could be widely used in the medical field. However, the semiconductor nature of these materials might

hinder their application as bio-cures. In order to test the feasibility of $Ce_xZr_{1-x}O_2$ nanoparticles scavengers in different working conditions, and better understand the science behind this semiconductor scavenger, the objectives in this thesis are as follows:

- Synthesize $Ce_xZr_{1-x}O_2$ nanoparticles applicable for free radical scavenging application
- Investigate the electronic property of $Ce_xZr_{1-x}O_2$ nanoparticles.
- Test the photocatalytic activity of $Ce_xZr_{1-x}O_2$ nanoparticles
- Explain the behavior of the materials

To achieve the objectives, $Ce_xZr_{1-x}O_2$ nanoparticles need to be synthesized via reverse micelle method using the same setup as Y.Y. Tsai's method [8, 9]. A direct comparison between the photocatalytic property and free radical scavenging activity of nanoparticles synthesized through the same route would give us a visual description of their characteristics. To assist the understanding of $Ce_xZr_{1-x}O_2$ nanoparticles behaviors, the electronic property of these particles need to be determined. As photocatalytic reactions often involve the generation of electron-hole pairs, the bandgap structure of the nanoparticles need to be measured. Also, to determine the performance of $Ce_xZr_{1-x}O_2$ nanoparticles under different working conditions, different UV light sources need to be applied. The catalytic activity is done via dye degradation method, which yields an accurate and fast result. The final results need to be correspondingly analyzed with other applications of $Ce_xZr_{1-x}O_2$ nanoparticles, which will help to build a mutual understanding of the overall system.

CHAPTER 2 BACKGROUND

2.1 Photocatalytic Materials

2.1.1 Basics of Semiconductor Photocatalysts

Photocatalysis is defined to be the chemical reaction induced by photo-irradiation with the presence of a catalyst [14]. The materials that could facilitate these reactions without being transformed are named photocatalysts. Photosynthesis by plants is a well-known example for photocatalysis, where chlorophyll serves the photocatalyst. There are different kinds of photocatalysts, such as organometallic complexes and semiconductors. They are being widely used in various fields environmentally and catalytically [15-18].

Semiconductor photocatalyst are exploited extensively nowadays for their optimal performance and non-pollutive nature. A number of photocatalytic reactions have already been applied for many practical uses, e.g. the removal of pollutants in water, self-cleaning glasses, etc. [15-18].

Theoretically all semiconductors can display photocatalytic properties due to the presence of a bandgap, but generally metal oxides and compounds exhibit better catalytic behaviors [19, 20]. Although extensively investigated for better performance in photocatalytic activity, the basic working principle of semiconductive photocatalysts is rather simple.

First a photon with energy higher than the bandgap of the material strikes on the sample. An electron in valence band (VB) is then excited to the conduction band (CB), leaving a hole in the VB with positive charge. The electron-hole pair is named an exciton. After the irradiation, the exciton either recombines and releases the absorbed photonic energy or it may react with chemicals present on the surface of photocatalyst to generate free radical species. During

reaction, photon energy and the excitons are consumed, while the structure of semiconductors remains unchanged. The whole reaction pathway is described in Figure 2-1.

Based on the above-discussed mechanism, several parameters in the reaction would contribute to the overall photocatalytic efficiency of a semiconductive material:

- light absorbing property of the semiconductor
- recombination rate of agitated electrons and holes
- rate for oxidative and reductive reactions that transform electrons and holes to free radicals

The light absorbing property is largely determined by the type and lattice structure of materials. Though sometimes surface modification could enhance the activity of photocatalysis, such an impact is negligible especially for powder materials.

The second and third factors decisive for photocatalysis should be considered accordingly. While the oxidative and reductive reactions on materials' surface contribute to photocatalysis, the recombination of excitons is destructive, producing nothing but heat to the whole system. However, though acting divergently to the photocatalysis efficiencies, both recombination progress and oxidation/reduction on the surface depend largely on the potential of those redox processes, which could be attributed to the band structure of a semiconductor.

Here titania [titanium dioxide, TiO_2], the most used semiconductor photocatalyst, is cited as an example to illustrate the effect of the two parameters. Figure 2-2 is a schematic diagram showing the potentials for various redox processes on TiO_2 surface from A. Fujishima et al. [21], the discoverer of titania-based photocatalysts. The main reactions and time needed for these processes are summarized as follows [22-24]:

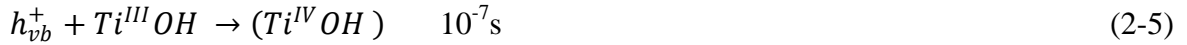
Exciton generation



Electron-hole trapping



Electron-hole recombination:



Oxidation and reduction:



From the equations it is easy to conclude that the rate of recombination is much higher than the rate of redox reactions and the photocatalytic activity of titania should be insignificant. However, the recombination rate could be retarded by various means. Researchers have successfully enhanced the catalytic activity of titania by doping with transition metals (e.g. Cr, Fe), coupling with metals (e.g. Pt) and coupling with a semiconductor (e.g. Aeroxide® TiO₂ P25: anatase phase titania with rutile phase titania).

On the other hand, if the recombination of excitons is enhanced, or the redox reactions on the surface are retarded, the photocatalytic activity of the material will be controlled.

2.1.2 Nanosize Impact on Semiconductor Photocatalysts

Due to the unique property of nanosize particles, the photocatalytic activity for these nanoparticles will deviate from, though still correlate to, their bulk counterparts. There have been many research reports focusing on the use of nanosize materials as photocatalysts [25-27]. These nanosize materials inhabit the region between single molecules and larger colloids, considered

parts of the bulk phase. They often exhibit unexpected behavior during application and it would be necessary to investigate them separately.

One size impact worthy to be noticed during photocatalysis is the quantum confinement effect. First discussed by Frohlich in 1937 [28-30], this size effect had been concluded in several reviews [31, 32]. It had a wide range impact on electrical, optical and photocatalytic properties of materials. Generally speaking, quantum confinement effect refers to the bandgap change or absorbance onset of a semiconductor due to the decrease of particle size. Specifically, when the particle size is comparable to the de Broglie wavelength of electronic carriers or excitonic Bohr radius, spatial confinement on carrier movements occurs. Correspondingly, quantization of energy levels and presence of discrete states could be expected. Consequently, the optical bandgap of the material will be increased. Quantum confinement effect often accompanies a blue shift in materials' absorption spectrum.

As quantum confinement is capable of "trapping" the electrons in discrete states, the redox potentials for photocatalysis reactions are subjected to a change. One factor need to be taken into account concerning the effect is the differential confining potential for electrons and holes [33]. Electrons are often more mobile than holes in most of the materials due to the different effective mass of these carriers. It is believed the critical size for quantum confinement effect is greatly influenced by the balance of different charge carrier mobility [33]. Whether such an impact would be beneficial or detrimental to photocatalytic reactions will be dependent on actual existing species.

On the other hand, nanosize particles display a much higher specific surface area than their bulk counterparts. As photocatalysis is a surface sensitive process, more surface sites will be

available for redox reactions and absorbing target reactants. In this aspect, nanosize materials would enhance the photocatalytic efficiency of catalyst on a same concentration basis.

2.2 Ceria and Cerium-Zirconium Dioxide Solid Solutions

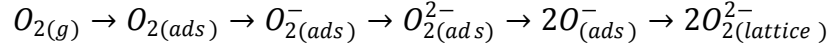
As has been discussed above, all semiconductor materials are theoretically potential photocatalysts. CeO₂ is a fluorite type semiconductor crystal with bulk bandgap estimated to be 3.16 eV [34]. That means a photo-irradiation with wavelength lower than 388 nm would be capable of intriguing the photocatalytic activity in bulk ceria compounds.

Actually, though not yet been intensively studied and used as photocatalysts, CeO₂ and CeO₂-based materials have already been exploited widely in various catalytic systems. The unique capability of exchanging lattice oxygen and environmental oxygen species due to their non-stoichiometric switch between Ce³⁺ and Ce⁴⁺ ionic states renders them effective catalysts as catalytic converters in automobiles, electrolytes in solid oxide fuel cells, gas sensors, etc. [14-20].

2.2.1 CeO₂ Nanoparticles in Biomedical Field

The biomedical use of CeO₂ nanoparticles was initially discovered by Rzigalinski et al. [35, 36], and confirmed by many other groups [8, 37, 38]. Different cultures and tissues were tested in vitro and in vivo. It was reported that the introduction of CeO₂ nanoparticles would extend lifespan of neuron cells up to six fold [35]. Other experiments dealing with different kind of cells were consistent with previous findings.

It is now believed by scientists that the protective effects CeO₂ nanoparticles have for living cells is due to their free radical scavenging capability. Though this property is not fully studied in living bodies, it has long been investigated in a variety of non-biological systems [5, 39]. As has been discussed above, CeO₂ have strong oxygen exchanging activity between lattice and environment. During these processes, oxygen radicals are generated as intermediates. The reaction pathway for oxygen as published by Tsai et al. is as follows [9]:



in which the process for oxygen molecules to be incorporated into ceria lattice is described. The oxygen molecules are subjected to a transformation through the intermediate state including peroxide and superoxide species before finally entering the lattice site oxygen ions, while the number of vacant site attributed to the existence of Ce^{3+} ions in ceria structure is also a function of oxygen pressure in the environment.

2.2.2 Cerium-Zirconium Solid Solutions

The ion exchange reactivity and oxygen storage capacity is highly limited for pure ceria system due to the equilibrium ratio between Ce^{3+} and Ce^{4+} ions in room temperature. To improve their free radical scavenging activity and protective power on living systems, scientists have selected zirconium to substitute cerium to achieve the enhancement [40].

Though found to be a relatively new concept in the biomedical field, $Ce_xZr_{1-x}O_2$ solid solution were studied as oxygen storage materials [6] and catalysts for soot decomposition [12]. Thus it has already been investigated by many research groups and its transitions between different phases have been confirmed.

Generally speaking, $Ce_xZr_{1-x}O_2$ solid solution would undergo three major phase transformations at room temperatures, according to Figure 2-4 [40]. A monoclinic phase is expected when the CeO_2 content is less than 10%, while a rigid cubic structure exists for these crystals with CeO_2 content more than 80%. Other than that, the solid solution displays tetragonal symmetry, which could be further divided into three stable and metastable phases. The presence of these different phases is suggested by XRD and Raman characterization [41, 42]. However, the boundaries for the transition between these phases rather approximate both due to the metastable nature of these phases and the size-sensitivity of structure distortions.

The structural change due to the introduction of zirconium substitutions also induces changes in stoichiometric properties within the crystals. Several studies have shown that the relative concentration of Ce^{3+} ions over Ce^{4+} ions in $\text{Ce}_x\text{Zr}_{1-x}\text{O}_2$ solid solution is promoted as the zirconium content increases, especially at high temperature [43, 44]. These non-stoichiometric changes are also confirmed by T. Sasaki et al. using electron diffraction pattern through TEM tests [45]. Thus the concentration of charge carriers is also subjected to an increase and so are their catalytic activities, theoretically.

2.3 Cerium-Zirconium Solid Solution Application in Free Radical Scavenging

Stated in Section 1.3, the objective of this thesis and research is to determine the photocatalytic activity of $\text{Ce}_x\text{Zr}_{1-x}\text{O}_2$ nanoparticles with free radical scavenging properties. Thus in this section, the previous study of free radical scavenging activity on these nanoparticles are briefly reviewed [9, 13].

Y.Y. Tsai et al. successfully synthesized a series of $\text{Ce}_x\text{Zr}_{1-x}\text{O}_2$ nanoparticles with uniform size distribution and well-defined crystalline state [13]. The synthesized CeO_2 nanoparticles were experimentally determined to be effective in improving the cell culture's viability by scavenging dangerous oxidative stress [9]. Zirconium substitution of cerium in the solid solution was proved to be beneficial in increasing the free radical scavenging capability for the synthesized nanoparticles. $\text{Ce}_x\text{Zr}_{1-x}\text{O}_2$ nanoparticles were determined to be efficient in scavenging peroxide and superoxide reactive oxygen species (ROS) in vitro, and the results were reproduced and summarized in Figure 2-6 [13]. It is suggested by Figure 2-6 that even compared to the currently commercialized ROS scavenger, superoxide dismutase (SOD) enzyme, $\text{Ce}_x\text{Zr}_{1-x}\text{O}_2$ nanoparticles with zirconium content more than 30% exhibited a better efficiency. Y.Y. Tsai et al. attributed the superior efficiency of $\text{Ce}_x\text{Zr}_{1-x}\text{O}_2$ nanoparticles to a higher mobile electronic carrier

concentration in the solid solutions and revealed an analogous trend between the free radical scavenging properties and oxygen storage capacities for these compounds.

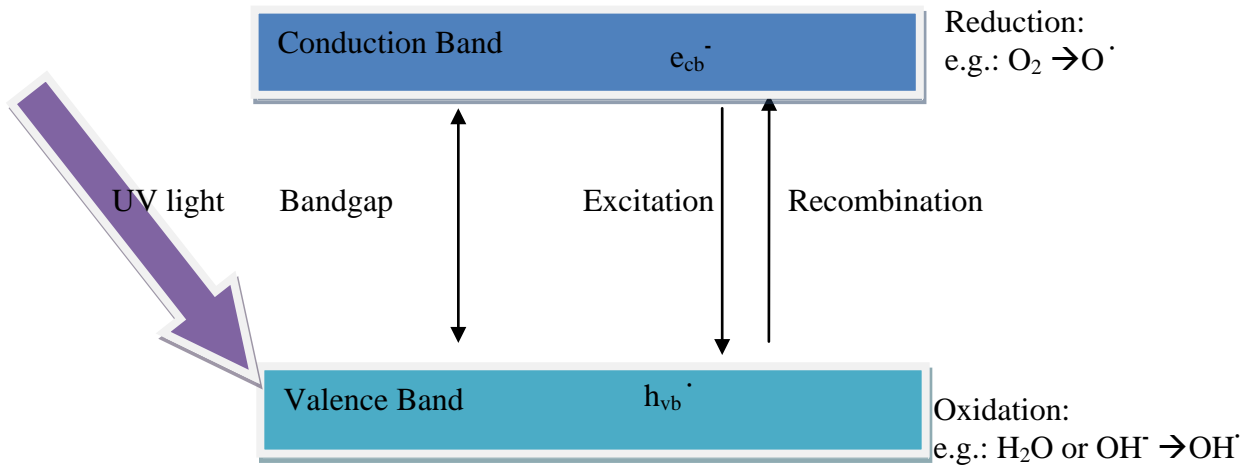


Figure 2-1. Schematic representation of the reactions taking place in a semiconductor photocatalyst

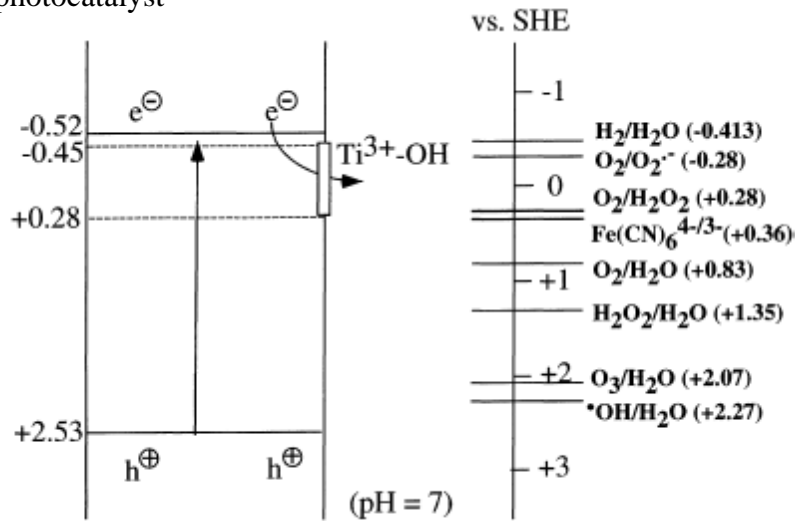


Figure 2-2. Schematic diagram showing the potentials for various redox processes occurring on the TiO_2 surface at pH 7

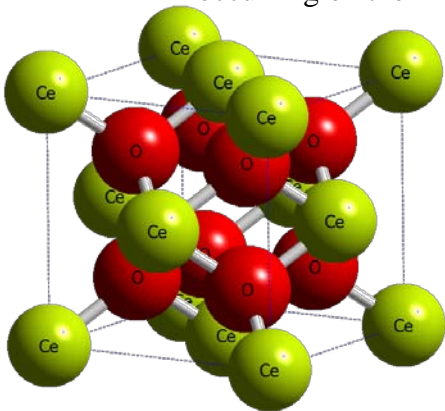


Figure 2-3. Schematic graph of CeO_2 fluorite structure

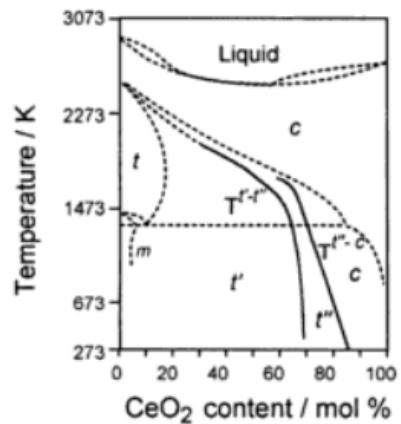


Figure 2-4. Phase diagram of $\text{Ce}_x\text{Zr}_{1-x}\text{O}_2$ system [26]

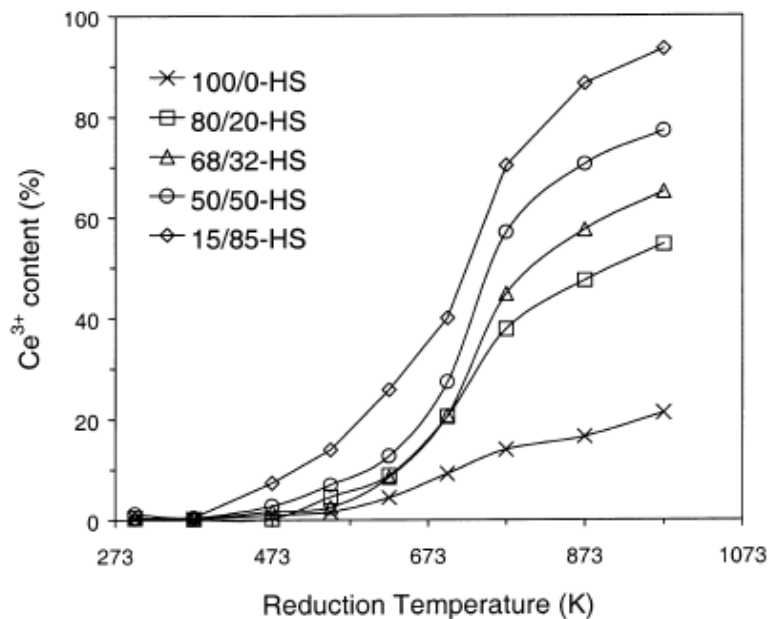


Figure 2-5. Reduction percentages of the $Ce_xZr_{1-x}O_2$ solid solutions as a function of reduction temperature (1 h at each temperature) ^[33]

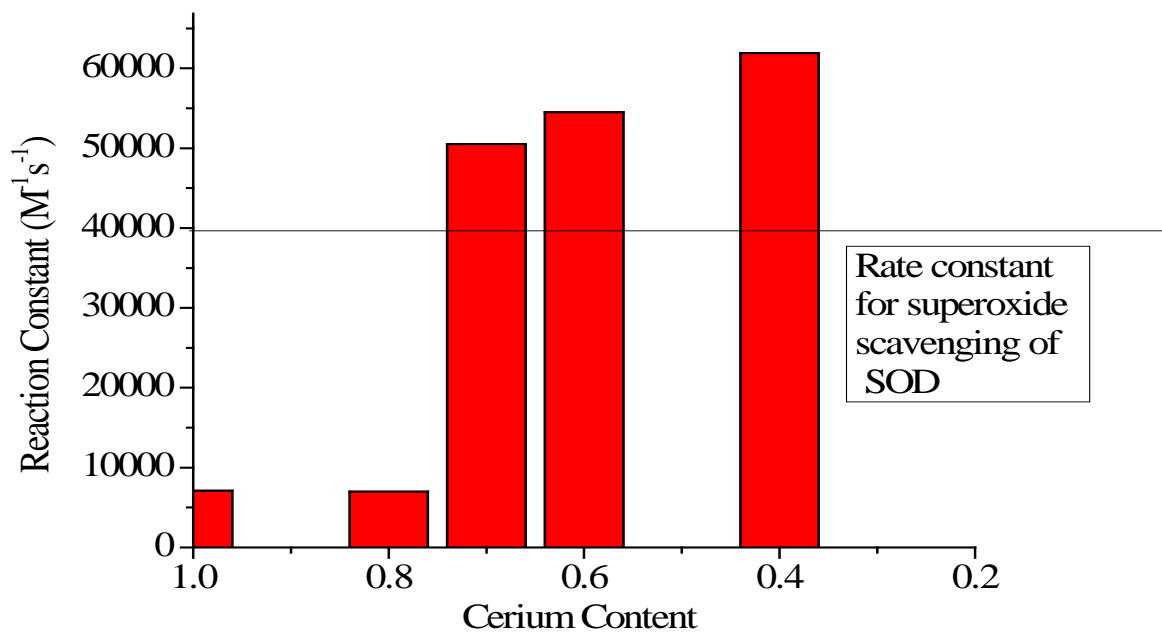


Figure 2-6. Rate constant for superoxide radical scavenging by $Ce_xZr_{1-x}O_2$ nanoparticles ^[13]

CHAPTER 3 SYNTHESIS OF CERIUM-ZIRCONIUM DIOXIDE NANOPARTICLES

In previous chapters, the main properties and applications of ceria and cerium-zirconium dioxide solid solution were reviewed. This chapter briefly introduces the preparation method used to synthesize the $Ce_xZr_{1-x}O_2$ nanoparticles in our group for photocatalysis tests. Overall, 2 steps were involved in the preparation: particles synthesis via reverse micelle method and the dispersion of nanoparticles in an aqueous system.

The synthesis of $Ce_xZr_{1-x}O_2$ nanoparticles would be a crucial step for precise evaluation of their photocatalytic property. To ensure a reliable analysis on the catalytic activity, the uniformity and homogeneity of $Ce_xZr_{1-x}O_2$ nanoparticles with various compositions needed to be maintained. Reverse micelle method could provide a system with relatively narrow range distribution of nanoparticles and better uniformity [46].

Saline/Tri-sodium citrate buffer was used to disperse the $Ce_xZr_{1-x}O_2$ nanoparticles. According to Dr. Y.Y. Tsai [9], the IEP (isoelectric point) of CeO_2 nanoparticles is subjected to a shift from pH=8 to approximately pH=2 when stabilized. The modification on the particles surface was believed to provide them sufficient electric double layer repulsion against agglomeration. The dispersed suspension was able to maintain its transparency for several months.

3.1 Reverse Micelle Method Synthesis

Reverse micelle method is considered to be one of the most suitable candidates for preparing highly size and surface-controlled nanosize particles [46]. A reverse micelle emulsion is a stable and isotropic mixture of oil, water and surfactant. Within the system, at least two immiscible phases co-exist with each other, while the surfactant molecules form a monolayer at the interface. The reverse micelle is so named because of the reverse alignment of surfactant

micelle surfaces. Where each micelle serves as a single isolated reactor, the formation of product particles is highly modulated. The achievable uniformity of synthesized nanoparticles and flexible control of their surface structure render reverse micelle method an ideal way in synthesizing various kind of particulate systems. Actually, it has already been applied widely to the preparation of quantum dots systems, such as CdSe [47], CdS [48-50], and ZnS–CdS alloys.

Presently, there are several water/oil systems applicable for reverse micelle method. Besides the commonly used AOT (Aerosol® OT)/toluene system, researchers have also applied NP-5 (Igepal CO-520)/cyclohexane solution [51] or even quaternary CTAB (Cetyl trimethylammonium bromide)/n-hexanol/heptanes [46] to form reverse micelles. By carefully controlling the [water]/[surfactant] ratio, [water]/[non-polar solvent] ratio and reaction time, nanoparticles with different features can be achieved [52].

3.2 Synthesis of $Ce_xZr_{1-x}O_2$ Nanoparticles

In our system, reagent grade zirconyl(IV) nitrate hydrate (99.5%, M.W.=231.23g/mol) and cerium(III) nitrate hexahydrate (99.5%, M.W.=434.22 g/mol) from Acros Organics were diluted to 0.1 M in aqueous system as precursor solution during the synthesis. 1.5M ammonium hydroxide was used as additives. Laboratory grade 100% solid sodium bis(2-ethylhexyl) sulphosuccinate Aerosol® OT from Fisher scientific was added into laboratory grade toluene to assist the formation of nano size reverse micelles. 1.5 g AOT solid was dissolved in 100ml toluene.

The precursor solution was prepared by mixing 0.1 mM cerium nitrate and 0.1 mM zirconyl nitrate aqueous solution according to their atomic ratio. 5 ml precursor was then titrated into the AOT/toluene solvent. The system was then stirred in a constant rate for 1 hr to allow the uniform generation of aqueous reverse micelles. After that, 10ml 1.5 M ammonium hydroxide solution was titrated into the system to initiate crystal nucleation and growth. The system was

then again stirred for 1 hour with constant rate for full reaction. The reaction and precipitation of the nanoparticles in the reverse micelle and was considered complete after this time. During the reaction, the system went through a brownish color and finally becoming yellowish, indicating the presence of cerium dioxide compounds. The reverse micelle reaction is described in Figure 3-1.

The synthesized particles in the reverse micelle system were then collected by centrifugation with an Eppendorf 5810 Centrifuge at 9400 rpm (rounds per minute) for 50 min. In order to remove AOT surfactant, the particles were then rinsed successively by methanol, ethanol and d.i. water (twice). The pollutants introduced in previous steps were washed away by d.i. water also. Finally, the purified particles were suspended and stabilized in a saline/tri-sodium citrate buffer solution for storage. The overall synthesis procedure is illustrated by Figure 3-2.

3.3 Particle Dispersion

0.05 M saline/tri-sodium citrate buffer solution made from solid state chemicals from MP Biomedical was prepared according to manufacturer's instruction. With a pH at around 7.4, the solution was used to disperse the synthesized $Ce_xZr_{1-x}O_2$ nanoparticles. Ultrasonication was used to break potential flocculation and assist dispersion. The stabilized nanoparticles in different solvents were shown in Figure 3-3. The dispersed nanoparticle system was able maintain their transparency for more than 6 month.

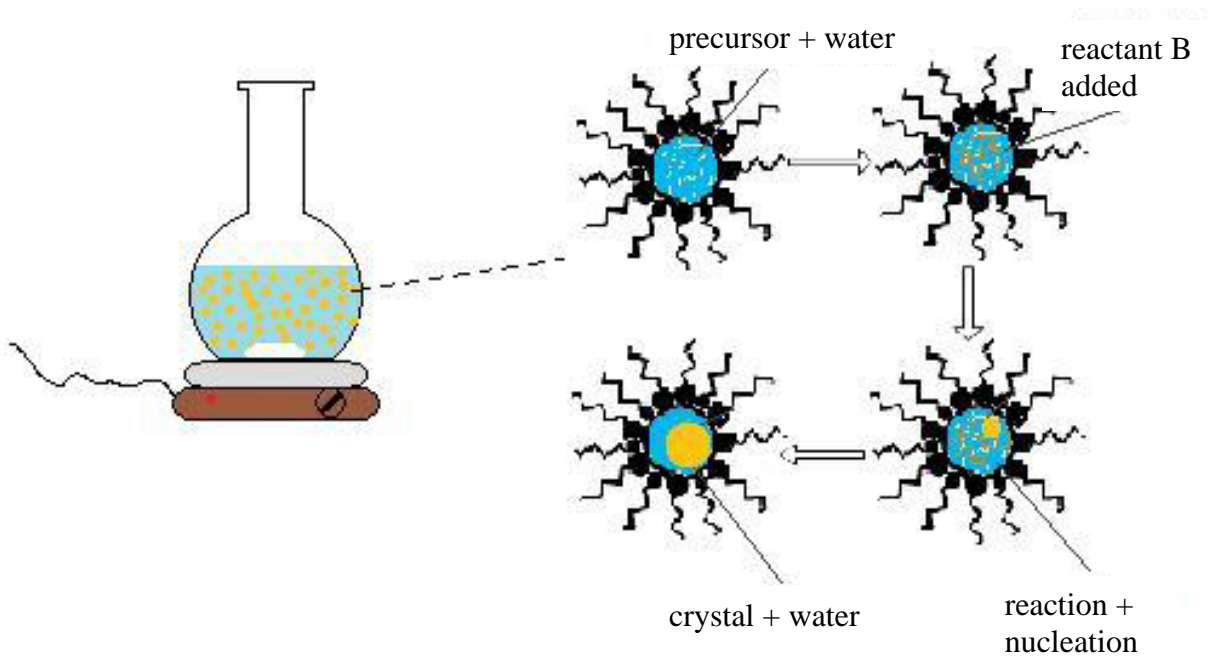


Figure 3-1. Schematic view of reverse micelle method

Step 1: Reverse micelle synthesis



Step 2: Particle wash and purification



Step 3: Particle dispersion



Figure 3-2. Overall procedure of $Ce_xZr_{1-x}O_2$ nanoparticles synthesis: A: reaction beaker on a magnetic stirrer; B: syringe used to titrate precursor and additive; C: precursor solution; D: eppendorf 5810 centrifuge; E: misonix S3000 ultrasonicator; F: washing solvents; G: dispersed nanoparticles.



Figure 3-3. Optical image: $Ce_xZr_{1-x}O_2$ suspensions in different solvents
(Left: S.C buffer Right: d.i. water)

CHAPTER 4 CHARACTERIZATION OF CERIUM-ZIRCONIUM DIOXIDE NANOPARTICLES

This chapter discusses the characterization of synthesized nanoparticles via a variety of techniques. Both the structural properties and electronic properties of the particulate system are to be presented. In this chapter, each technique used to determine the characteristics of particles will be briefly introduced. The results from these characterization techniques will also be displayed.

4.1 Chemical Ratio Determination

4.1.1 Inductively Couple Plasma Spectrometry (ICP)

Inductively Coupled Plasma Spectrometry is a sophisticated analytical technique aiming to detect the trace materials in target samples. Inductively coupled plasma refers to a plasma source where the energy is supplied by electromagnetically induced electrical currents. An ICP typically consist of several components: a sample introduction system, a torch, high frequency generator, transfer optics and spectrometer and a computer interface. A torch in ICP is comprised by three concentric tubes, usually made from silica. The torch is situated with a water-cooled coil of radio frequency magnetic field generator. During operation, a flow of argon gas is introduced into the torch, where the radio frequency field activates the electrons and their collision with argon gas makes them electrically conductive [53, 54].

Thus the plasma within the torch contains mostly argon atoms with a small proportion of free electrons and argon ions. The temperature of the plasma is rather high. In order to prevent possible detrimental damage to other parts of the instrument, the plasma is insulated by several flows of inert gas, typically argon and nitrogen [55, 56].

In ICP experiments, it requires the elements to be in a solution state before entering the instrument. Normally an aqueous system is preferred. During operation, the sample solution is

introduced into the system by a carrier gas (argon, sometimes helium). Then the target elements are injected into the argon plasma and ionized. Atomic emission of the samples is converted into electrical signal by means of diffraction grating. The light intensity with different wavelength is monitored by photomultiplier. As each element has specific value of emission lines in the argon plasma, the electrical signal of these lines are compared with standard sample with known concentrations. By comparing the intensity of standards and target samples the concentration of specific elements are to be determined.

4.1.2 Compositional Results

Perkin-Elmer Plasma 3200 Inductively Coupled Plasma Spectroscopy (ICP) in Particle Engineering Research Center (PERC) was used to confirm the actual chemical composition of our samples. To prepare solution feasible for ICP analysis, 200 ml particles suspension was allowed to be fully dissolved by sulfuric acid (95%, Sigma-Aldrich) overnight, and then diluted with same amount of deionized water. The ionic concentration of cerium over zirconium in the solution was determined afterwards in plasma state. The standard deviation of the measurements was established by 1 ppm, 10 ppm and 100 ppm cerium and zirconium ICP standards provided by Ricca Chemical. The detection limit of the equipment was less than 1ppm.

The chemical ratio of final products is shown in Table 4-1. “Formula” column indicated the expected formulation of the product based on the reagent ratio. From the results shown in the table, it was suggested that though a deviation no more than ± 0.06 was achieved away from the calculated formula, the actual component of the nanoparticles generally correspond well with theoretical formulation. The deviation could either be induced during the process of synthesis or from the experimental error in ICP equipment. Generally speaking, the overall quality of the particles was acceptable for further analysis in characterizing the photocatalytic activities of particles with distinguishable components.

For comparison purpose, the atomic ratios for commercial particles used in parallel experiments, directly reported from their companies, were also included in the table.

4.2 Particle Size Analysis

4.2.1 Dynamic Light Scattering Method

In this section dynamic light scattering method is described as it was applied to evaluate the size and size distribution of $\text{Ce}_x\text{Zr}_{1-x}\text{O}_2$ nanoparticles. The hydrodynamic diameter of equivalent sphere to the nanoparticles are measured and reported.

Dynamic light scattering is a commonly used technique for determining size and size distribution of small particles in suspensions [57]. The fundamental for this technique is the random movement of particles due to their collision with solvent molecules, also known as Brownian motion. The velocity of Brownian motion could be defined by the translational diffusion coefficient of particles, and it is indirectly proportional to the size of particles. When an impinging laser hits suspended particles sufficiently small, they are to be scattered in different directions. Depending on the movement of the target particles, the coherent scattering light could either be constructive or destructive to the impinging light [58], as shown in Figure 4-1. The fluctuation in intensity of the light is collected by a correlator. Given sufficient time, an autocorrelation function could be plotted from the random motion of small particles. By fitting the intensity curves the size and size distribution of particles are able to be obtained. Normally, larger particles often display a smooth curve and smaller ones have more noisy curves.

However, by applying the technique it is worthy to be aware that dynamic light scattering is actually measuring the hydrodynamic diameter of the particle. The hydrodynamic diameter consists of both the particles diameter and thickness of electrical double layer. The impact of electrical double layer on the results depends on the impact it has on the motion of the particles. Also, the hydrodynamic diameter is determined based on the equivalent sphere of target particles.

Thus it might not be applicable for those particles with high aspect ratio, where the ease of motion for different directions is highly different.

4.2.2 Size and Size Distribution of $Ce_xZr_{1-x}O_2$ nanoparticles

Figure 4-2 showed the size and size distribution results of synthesized $Ce_xZr_{1-x}O_2$ nanoparticles from Nanotrak Particle Size Analyzer in PERC. Both frequency and cumulative frequency for the particles were included in the diagrams as a function of diameter. Except for the zirconia particles, all the particles synthesized with our setup displayed a generally narrow range distribution at around 4 nm but no more than 10 nm. From the cumulative frequency curves d_{50} and d_{95} for those compounds were also determined and reported in Table 4-2. The equivalent sphere diameters based on mean-area and mean-volume was calculated in the table. Specific surface area (SSA) was critical in this research as photo-assisted reactions were often surface-dependent, involving both chemical adsorption on the particles and reaction process. The theoretical SSA was related to d_{NS} and d_{NV} with the equation:

$$SSA = \frac{A}{\rho \times V} (m^2/g) \quad (4-1)$$

In which A was the total area of the sample, V was the corresponding volume and ρ was the density which could be calculated by 1st order Vegard's law with reported density of ceria and zirconia. From the calculation, SSAs of $Ce_xZr_{1-x}O_2$ nanoparticles were determined to be 109 ± 20 m²/g, approximately two times of the reported SSA of 50 ± 15 m²/g for Aeroxide® TiO₂ P25 from Evonik Corporation and NanoActive Cerium Oxide. However, in this table, the theoretical SSA for zirconia was not included. It was mainly because of a relatively agglomerated state of zirconia particles, which had been discovered in TEM images. Furthermore, they did not exhibit a single-crystalline state according to the electron diffraction

pattern, which will be covered in a latter part of this chapter. Thus the SSA for these particles could not be simply calculated as had been done to nanoparticles with other compositions.

For comparison purposes, the corresponding data for commercial particles used in parallel experiments, directly reported from their companies, were also included in Table 4-2.

4.3 Structural Characterization by TEM

4.3.1 High-Resolution Transmission Electron Microscopy

In this section, High-Resolution Transmission Electron Microscopy (HR-TEM) data is reported, which is applied to determine the particle shape, crystal structure and crystallinity of $\text{Ce}_x\text{Zr}_{1-x}\text{O}_2$ nanoparticles.

TEM is a scientific instrument that utilizes transmitted electrons instead of light to scrutinize objects at very fine resolutions [59]. When a high-energy electron passes through the specimen, it interacts with the sample and yields signals representing the information it has collected. There are two main modes applicable in TEM technique: image mode and diffraction mode. By adjusting the intermediate lenses, different portions of electrons that pass through the back focal plan will be collected. Either the second image of the sample or a diffraction pattern will be obtained on the image screen like photographic film or CCD camera.

For image mode, contrast is generated directly by surface absorption of electrons on the sample. The thicker the sample, or the higher the atomic number the sample has, the darker the image will be. If there is the sample in the beam path the image will appear to be bright. Thus it is also named “bright field” imaging [60].

For diffraction mode, DeBroglie’s model is used to explain the behaviors of electrons. With the initial acceleration through electric field, electrons could be considered as a wave with equivalent wavelength described by Equation 4-2:

$$\lambda = \frac{h}{p} = \frac{h}{\sqrt{2meV}} \quad (4-2)$$

where h is Planck's constant; p is momentum; m is the mass for an electron; e is the electron charge and V is the acceleration voltage. By substituting real values in Equation 4-2:

$$\lambda \text{ (nm)} = \sqrt{\frac{1.505}{V \text{ (Volts)}}} \quad (4-3)$$

Similar as other types of diffraction techniques, such as XRD (X-Ray Diffraction), LEED (Low Energy Electron Diffraction) and RHEED (Reflective High Energy Electron Diffraction), the diffraction in TEM follows Laue's rule and only dots on Ewald's sphere in reciprocal lattice are able to be displayed. Thus it is easy to conclude diffraction pattern with distinguishable rings have better crystallinity than ones with diffusive "lunar" pattern. For a large single crystal, discrete diffraction spots will be displayed in the pattern.

4.3.2 TEM Results and Discussion

Figure 4-3 to Figure 4-5 represented the selected TEM graphs of $\text{Ce}_x\text{Zr}_{1-x}\text{O}_2$ nanoparticles ($x=1, 0.6, 0$). Both their bright field image and electron diffraction pattern were included. As the nanoparticles were synthesized using the same method as in Dr. Y.Y. Tsai's dissertation, only three distinguishable compositions were chosen for the TEM test.

The bright field images of CeO_2 and $\text{Ce}_{0.6}\text{Zr}_{0.4}\text{O}_2$ nanoparticles displayed generally uniform shape with size around 2-3 nm. Some selected crystallites were highlighted with red circles. The relatively uniform sphere-like shape of the particles proved the feasibility of dynamic light scattering method. It was suggested from the lattice fringes that each nanoparticle exhibited a single-crystalline state. The distinguishable rings in electron diffraction pattern also proved the well-defined crystallinity within the samples. However, for ZrO_2 samples, the particles seemed to be highly agglomerated with porous structure. It was believed that the difference of interaction between oxide particles and the surfactant (sodium citrate buffer) caused

the divergent behaviors between ZrO₂ and other compounds. The diffusive electron diffraction pattern also indicated a poor crystalline state within ZrO₂ particles. Due to the agglomeration and the deviation of diameter measured by dynamic light scattering method resulting from the non-uniformity of ZrO₂ particles, the SSA was not calculated in Table 4-2.

4.4 Structural Characterization by XPS

4.4.1 X-Ray Photoelectron Spectroscopy

To confirm the actual bonding state and chemical shift due to the variation of composition and UV radiation, X-Ray Photoelectron Spectroscopy (XPS) was used for the synthesized nanoparticles.

Also known as Electron Spectroscopy for Chemical Analysis (ESCA) [61], XPS is a semi-quantitative, surface sensitive [62] technique based on the high-energy version of photoelectric effect, allowing both chemical and elemental identification of compounds. XPS could detect all elements except for hydrogen and helium with concentration higher than 0.1 atomic%. During operation, X-ray with energy of 1~2 keV is generated and impinge on the sample, penetrating several microns below the surface; incident X-ray photon interacts with an core-level electron of an atom, while energy of the X-ray photon is transferred to the electron; the electron with sufficient energy is then ejected from the atom and collected by an electron energy analyzer. The energy of excited electron could be described by Equation 4-3:

$$h\nu = I_k + E_k + \Phi \quad (4-4)$$

where $h\nu$ is the photonic energy of primary x-ray; I_k is the binding energy of a core electron; E_k is the kinetic energy of ejected electron and Φ is the work function of the equipment (3~4 eV).

To prevent contamination and provide an unobstructed path for the generated photoelectrons, XPS system is operated under an ultra-high vacuum ($\leq 10^{-9}$ Torr). Thus sample must be stable in the chamber, either in a solid state or undergoing extra pre-treatment.

4.4.2 Experimental

The well suspended $Ce_xZr_{1-x}O_2$ ($x=1, 0.4$) nanoparticles were re-dispersed in ethanol and collected by centrifuge. To ensure there was no more sodium-citrate group bounded to the particle surface, the particles were washed by ethanol twice. Finally, particles suspension in ethanol was dipped on to a $1\text{cm}\times 1\text{cm}$ square cut silicon substrate. After the evaporation of ethanol, the nanoparticles were deposited on the substrate. Multi-layer atoms were applied to substrate to ensure there was sufficient sample to generate XPS signals.

In order to determine the change in structure attributed to UV radiation, another CeO_2 sample pre-treated with UV light was prepared. 20ml sample and $20\ \mu\text{l}$ 5000 ppm Procion® MX-5B dye used for the photocatalysis experiment, which will be introduced in Chapter 5, were added into a transparent glass vial, and placed in reaction chamber for 6 hours. 302 nm UV light was used as irradiation source. After that, the samples were prepared with same routine as has been described above to make deposition on silicon substrates.

4.4.3 Results and Discussion

By integrating the area under corresponding XPS peaks, the relative intensity of each element is able to be achieved. Table.4-3 summarizes the intensity of carbon 1s, cerium 3d and oxygen 1s peaks for unirradiated CeO_2 , unirradiated $Ce_{0.4}Zr_{0.6}O_2$ and irradiated CeO_2 , respectively. From the cerium/oxygen equivalent ratios calculated from the integration, it is easy to suggest, though not quantitatively, that the substitution of cerium by zirconium would favor the generation of Ce_2O_3 bonding states, increasing the concentration of oxygen vacancies in the CeO_2 lattice, while in the other case, UV irradiation would contribute to the incorporation of environmental oxygen species into CeO_2 lattice sites and eliminate its intrinsic non-stoichiometric defects.

4.5 Electronic Properties Characterization by UV/Visible Spectroscopy

4.5.1 Absorption Spectrum by UV/Visible Spectroscopy

UV/Visible spectroscopy is a spectroscopic technique commonly used to examine the solid or solution of transition metal ions or organic compounds. It utilizes the electronic transition from ground state to an excited state for target compounds. Within the transition, electrons are promoted from valence band to the conduction band after absorbing the energy in an impinging photon. Only photons with energy that match the energy gap between molecular orbitals are to be absorbed, and an absorption peak is generated in the spectrum. Though this information is also displayed more or less by the color of the samples, a UV/VIS measurement will allow a more precise quantitative determination of samples' properties.

The concentration of samples and the readings of UV/VIS are correlated by Beer-Lambert's Law, shown in Equation 4-4:

$$A = -\log_{10}\left(\frac{I}{I_0}\right) = \alpha \times c \times l \quad (4-5)$$

where A is the measured absorbance; I and I_0 are the transmitted and original intensity of light, respectively; α is the extinction coefficient; c is the concentration of the sample; l is the length of light path. Beer-Lambert's Law is applicable for most homogeneous samples. With UV/VIS, the type of functional groups, the concentration of certain species and many other information could be obtained.

In this section, the absorption spectra of $\text{Ce}_x\text{Zr}_{1-x}\text{O}_2$ nanoparticles were measured by Perkin-Elmer Lambda 800 UV/Vis spectrometer. Before the experiment, the $\text{Ce}_x\text{Zr}_{1-x}\text{O}_2$ nanoparticles were diluted to a concentration of 0.75 mM and titrated into quartz cuvettes for scanning. The scanning range was 220 nm to 800 nm. For comparison purpose, commercial NanoActive Cerium Oxide particles from NanoScale corporation were also included.

Figure 4-6 showed the absorption spectra for $Ce_xZr_{1-x}O_2$ nanoparticles with different compositions ($x=1, 0.8, 0.7, 0.6, 0.4, 0.2, 0$). In the diagram, a strong blue shift of the absorption edge was presented with increasing zirconium component. While for metals, absorption peaks was correlated to the interband transition of electrons, for semiconductors, the position of absorption edge is determined by separation between valence band and conduction band. Also, with increasing zirconium component, the ability of absorbing UV light was also decreasing. This corresponded well to the UV absorbing ability of ceria nanoparticles. However, surprisingly, despite that the absorption edge was moved to a lower energy position, a lower intensity of absorption peak for commercial ceria was displayed in the diagram. This might be caused by the relatively lower surface area available on commercial ceria in the same concentration of synthesized $Ce_xZr_{1-x}O_2$ nanoparticles.

4.5.2 Tauc Relation and Bandgap Calculation

To better understand the electronic property and their performance under UV light, the bandgap of the nanoparticles were also calculated from their absorption curves. According to the Tauc relation, the absorption coefficient (extinction coefficient) is related to the bandgap of a semiconductor material with Equation 4-5 [34, 63]:

$$\alpha(h\nu) = A(h\nu - E_g)^{m/2} \quad (4-6)$$

where A is a constant, α is the absorption coefficient; $h\nu$ is the photonic energy; E_g is the bandgap of the sample; $m=1$ for direct band transitions and $m=4$ for indirect band transitions [64].

In following calculation $m=1$ and it is presumed for a direct band transition in ceria. Figure.4-7 displayed the plot of $(\alpha h\nu)^2$ versus $h\nu$ transformed from UV/VIS curves. The energy intercept of fitted line with x axis yielded the E_g value for the sample.

The E_g values for each synthesized nanoparticles are summarized in Table 4-3. Although bulk ceria had only an $E_g=3.19$ eV [34], nanosize ceria particles displayed a much larger bandgap $E_g=3.58$ eV. These might be attributed to the effect of quantum confinement. Due to the lack of sufficient electrons in each single energy state, the electrons were restrained to the potential wells in lateral dimensions so that quantized energy levels took place of continuous bands structure in these nanoparticles. The relationship between quantum confinement and particle size could be inferred by the contrast between commercialized NanoActive ceria and synthesized ceria in our lab. The commercial ceria had a larger crystallite size of 7nm, and correspondingly exhibited a smaller bandgap than ceria obtained from reverse micelle method. Thus a smaller crystal would induce a more severe quantum confinement effect in the experiments. Also, it can be seen from Table 4-3 that the bandgap energy exhibited an increasing trend as the ratio of zirconium in the oxide increased. This corresponded to the fact that zirconia ($E_g=4-5$ eV depending on the synthesis method) has a much larger bandgap than ceria. The non-linear increase of bandgap could be explained by a higher-order Vegard's law as a result of bowing effect.

Table 4-1. Cerium/Zirconium ratio for synthesized $Ce_xZr_{1-x}O_2$ nanoparticles by inductively coupled plasma

Formula	Cerium atomic ratio	Deviation % (Cerium)	Zirconium atomic ratio	Deviation % (Zirconium)
Commercial Ceria	>0.997*	—	—	—
Aeroxide [®] TiO ₂ P25	≥0.995	—	—	—
CeO ₂	0.97	0.036	0.03	0.075
Ce _{0.8} Zr _{0.2} O ₂	0.78	0.046	0.22	0.044
Ce _{0.7} Zr _{0.3} O ₂	0.70	0.036	0.30	0.037
Ce _{0.6} Zr _{0.4} O ₂	0.58	0.057	0.42	0.038
Ce _{0.4} Zr _{0.6} O ₂	0.34	0.20	0.66	0.037
Ce _{0.2} Zr _{0.8} O ₂	0.16	0.14	0.84	0.034
ZrO ₂	0.03	0.99	0.97	0.036

Table 4-2. Size and specific surface area of $Ce_xZr_{1-x}O_2$ nanoparticles by dynamic light scattering method

Comparison Sample*	d ₅₀ (μm)	Average crystallite size(nm)	Specific surface area: SSA(m ² /g)		
Commercial Ceria	9.5	7	7	>=50	
Aeroxide [®] TiO ₂ P25	—	21	21	50±15	
Sample	d ₅₀ (nm)	d ₉₅ (nm)	Area mean diameter: d _{NS} (nm)	Volume mean diameter: d _{NV} (nm)	Specific surface area: SSA(m ² /g)
CeO ₂	3.0	4.0	3.6	3.6	116
Ce _{0.8} Zr _{0.2} O ₂	2.6	4.4	3.4	3.6	107
Ce _{0.7} Zr _{0.3} O ₂	3.5	4.9	4.3	4.5	89
Ce _{0.6} Zr _{0.4} O ₂	3.2	4.5	3.8	3.9	109
Ce _{0.4} Zr _{0.6} O ₂	3.0	4.1	3.5	3.6	123
Ce _{0.2} Zr _{0.8} O ₂	2.9	4.3	3.5	3.6	128
ZrO ₂	75.9	148.9	106.9	118.2	—

* These data were directly reported from their company

Table 4-3. XPS data for CeO₂ and Ce_{0.4}Zr_{0.6}O₂ nanoparticles.

Sample	C 1s		Ce 3d		O 1s		Ce/O equivalent area ratio
	Height	Area	Height	Area	Height	Area	
unirradiated CeO ₂	2305	13185	11665	86806	13001	51703	1.679
unirradiated Ce _{0.4} Zr _{0.6} O ₂	4885	22402	10890	72381	20888	69782	2.593
irradiated CeO ₂	2155	11028	9629	61705	15922	57939	1.065

Table 4-4. The calculated bandgap for direct band transition of $\text{Ce}_x\text{Zr}_{1-x}\text{O}_2$ nanoparticles.

Sample	Bandgap (eV)
Commercial CeO_2	3.40 ± 0.06
CeO_2	3.58 ± 0.03
$\text{Ce}_{0.8}\text{Zr}_{0.2}\text{O}_2$	3.69 ± 0.02
$\text{Ce}_{0.7}\text{Zr}_{0.3}\text{O}_2$	3.70 ± 0.02
$\text{Ce}_{0.6}\text{Zr}_{0.4}\text{O}_2$	3.70 ± 0.04
$\text{Ce}_{0.4}\text{Zr}_{0.6}\text{O}_2$	3.73 ± 0.05
$\text{Ce}_{0.2}\text{Zr}_{0.8}\text{O}_2$	3.83 ± 0.01
ZrO_2	4.55 ± 0.09

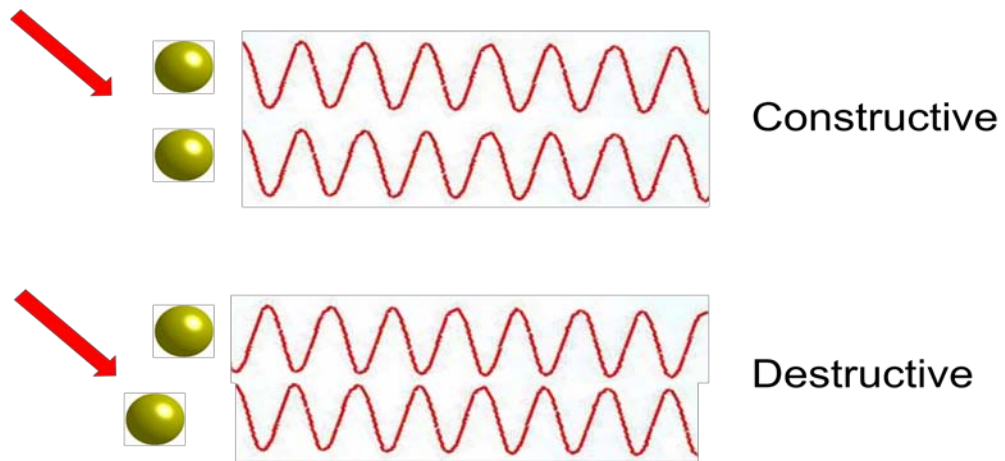


Figure 4-1. Constructive and destructive effect of light scattering

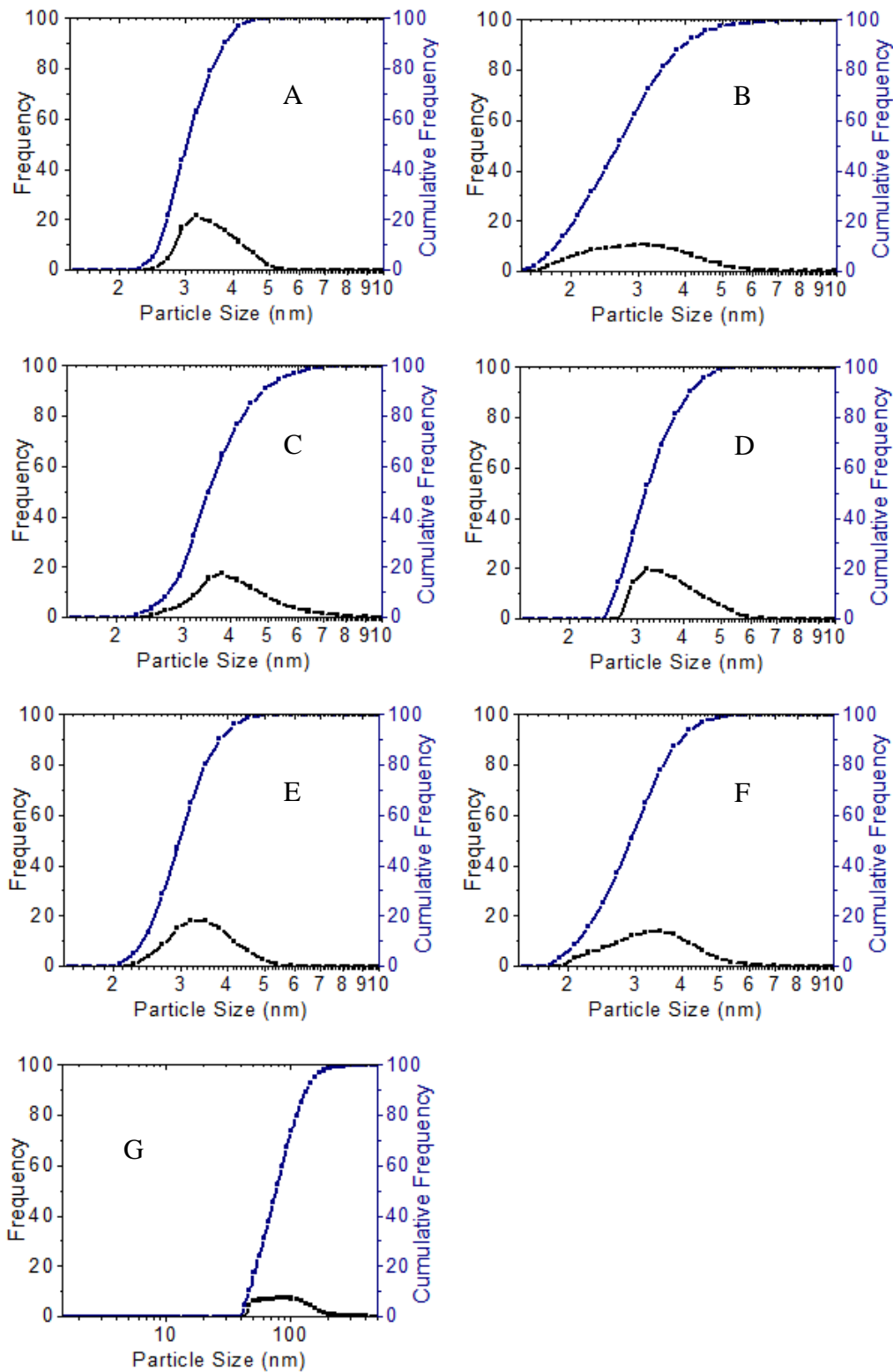


Figure 4-2. Size and distribution of $\text{Ce}_x\text{Zr}_{1-x}\text{O}_2$ nanoparticles by dynamic light scattering method. A: CeO_2 ; B: $\text{Ce}_{0.8}\text{Zr}_{0.2}\text{O}_2$; C: $\text{Ce}_{0.7}\text{Zr}_{0.3}\text{O}_2$; D: $\text{Ce}_{0.6}\text{Zr}_{0.4}\text{O}_2$; E: $\text{Ce}_{0.4}\text{Zr}_{0.6}\text{O}_2$; F: $\text{Ce}_{0.2}\text{Zr}_{0.8}\text{O}_2$; G: ZrO_2 .

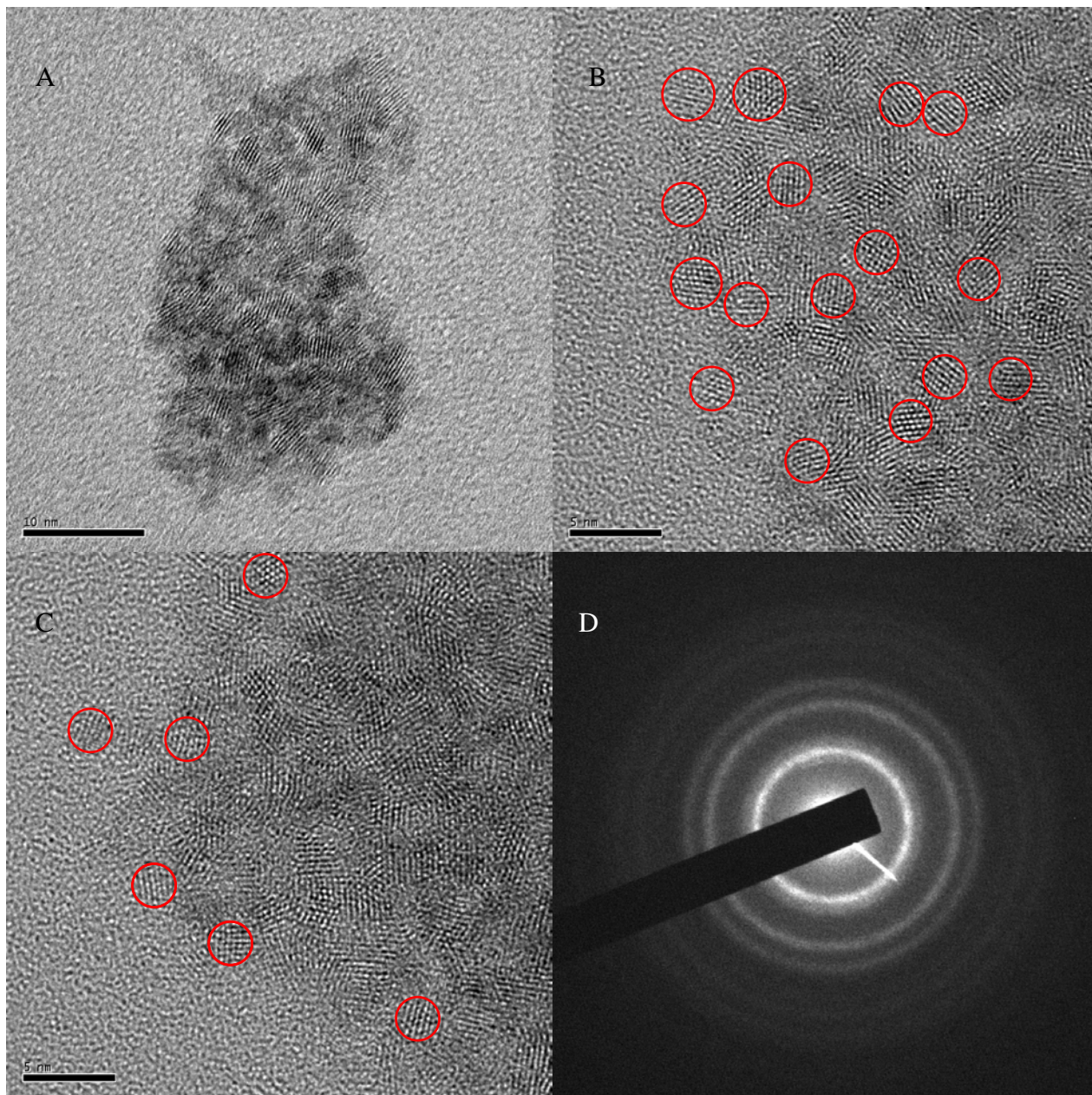


Figure 4-3. TEM image of CeO₂ nanoparticles: A: CeO₂ nanoparticles at magnification 400000X, scale bar 10nm; B: CeO₂ nanoparticles at magnification 600000X, scale bar 5nm; C: CeO₂ nanoparticles at magnification 600000X, scale bar 5nm; D: electron diffraction pattern of CeO₂ nanoparticles.

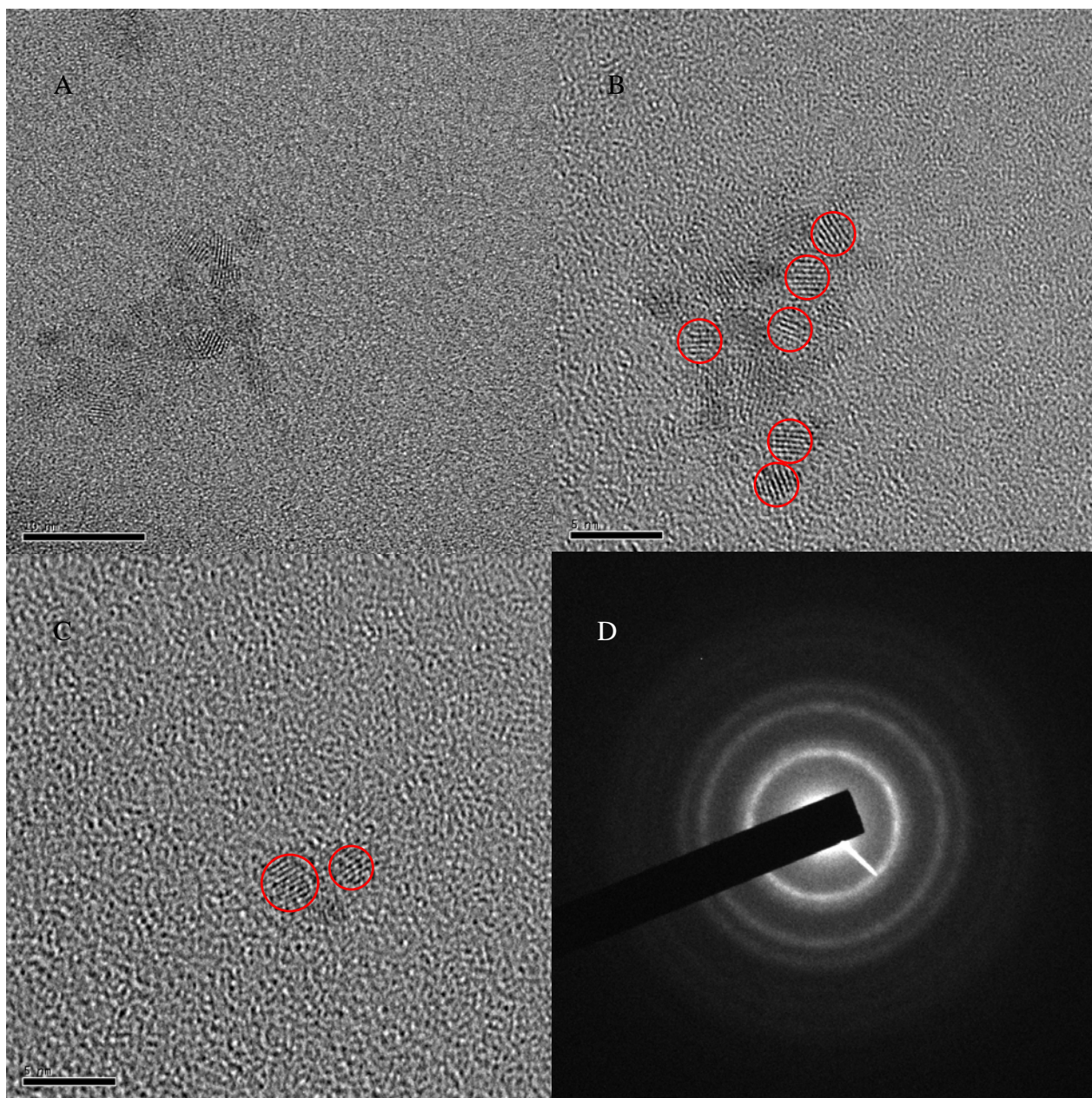


Figure 4-4. TEM image of $\text{Ce}_{0.6}\text{Zr}_{0.4}\text{O}_2$ nanoparticles: A: $\text{Ce}_{0.6}\text{Zr}_{0.4}\text{O}_2$ nanoparticles at magnification 400000X, scale bar 10nm; B: $\text{Ce}_{0.6}\text{Zr}_{0.4}\text{O}_2$ nanoparticles at magnification 600000X, scale bar 5nm; C: $\text{Ce}_{0.6}\text{Zr}_{0.4}\text{O}_2$ nanoparticles at magnification 600000X, scale bar 5nm; D: electron diffraction pattern of $\text{Ce}_{0.6}\text{Zr}_{0.4}\text{O}_2$ nanoparticles.

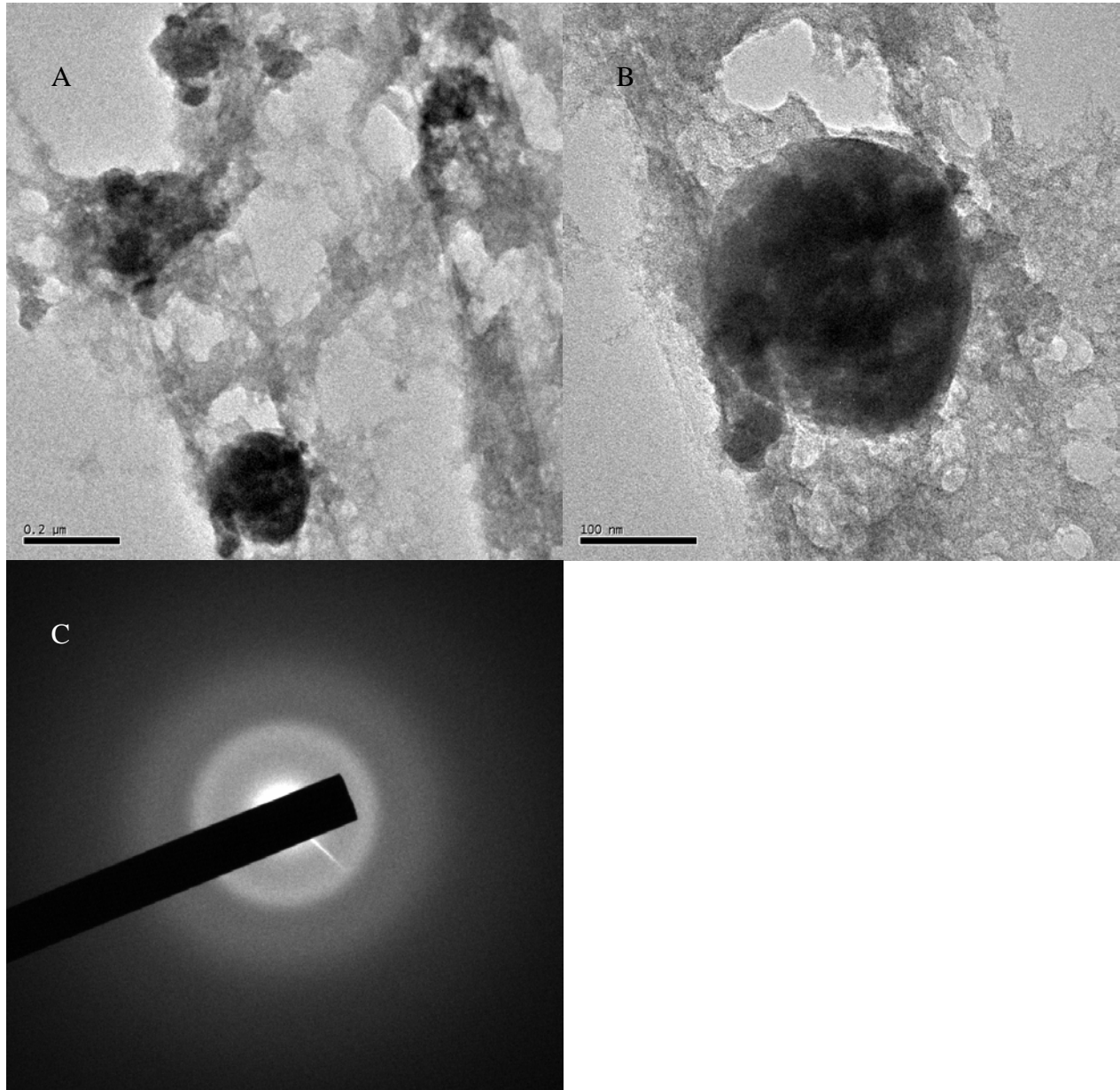


Figure 4-5. TEM image of ZrO_2 particles: A: ZrO_2 particles at magnification 15000X, scale bar 10nm; B: ZrO_2 particles at magnification 40000X, scale bar 5nm; C: electron diffraction pattern of ZrO_2 particles.

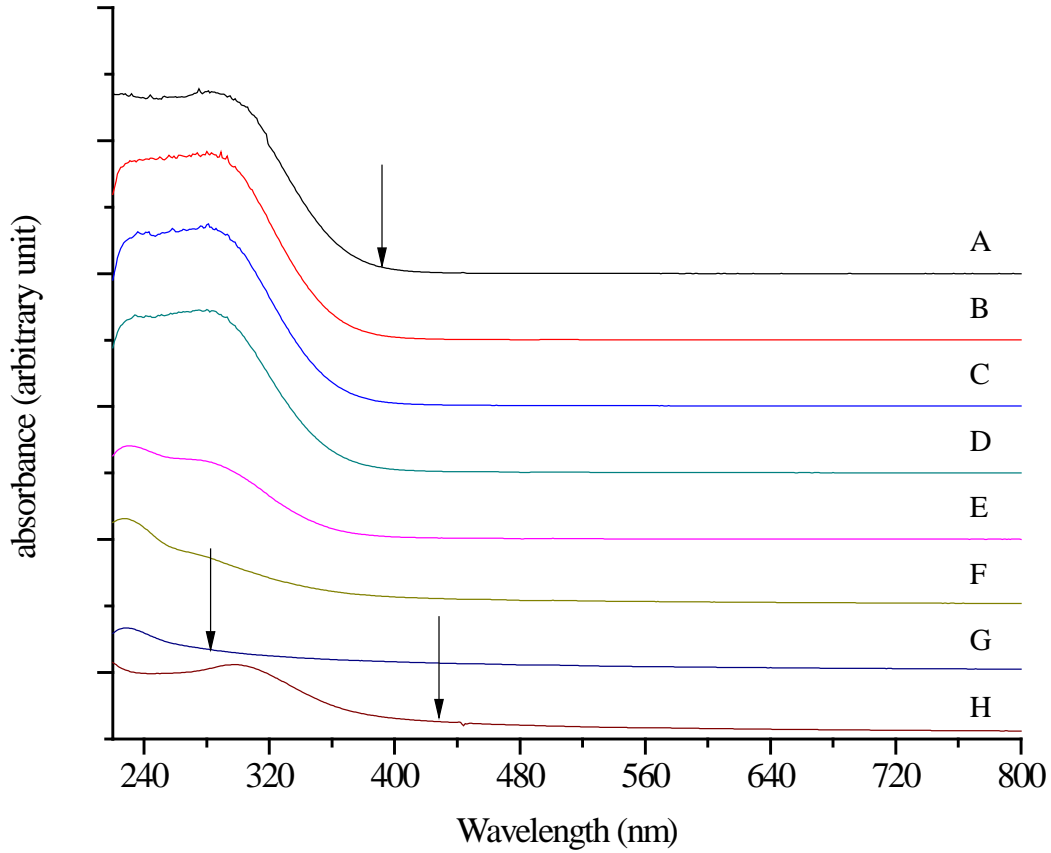


Figure 4-6. UV/VIS absorption spectra for synthesized $Ce_xZr_{1-x}O_2$ nanoparticles. A: CeO_2 ; B: $Ce_{0.8}Zr_{0.2}O_2$; C: $Ce_{0.7}Zr_{0.3}O_2$; D: $Ce_{0.6}Zr_{0.4}O_2$; E: $Ce_{0.4}Zr_{0.6}O_2$; F: $Ce_{0.2}Zr_{0.8}O_2$; G: ZrO_2 ; H: NanoActive Cerium Oxide

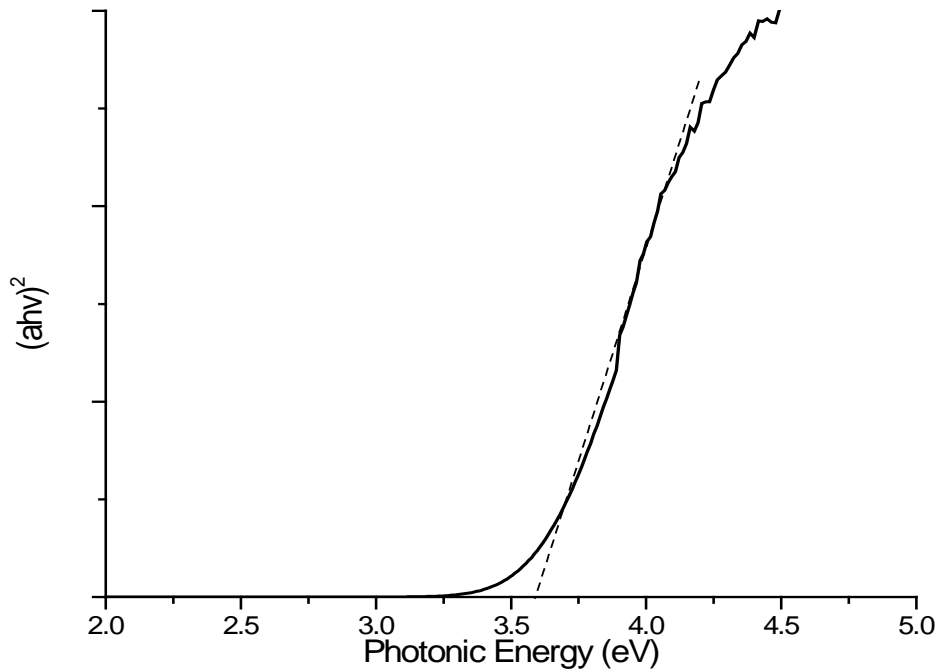


Figure 4-7. Fitting curve for direct band transition of ceria nanoparticles.

CHAPTER 5 PHOTOCATALYSIS BY CERIUM-ZIRCONIUM DIOXIDE NANOPARTICLES

In this chapter, experiments performed to determine the photocatalytic activity of $Ce_xZr_{1-x}O_2$ nanoparticles are described. Dye degradation method was used to achieve the objectives [65, 66]. In the experiments an organic dye was photocatalytically degraded and its concentration was monitored as a function of time. This technique was chosen over other tests mainly because of its fastness, accuracy and particle property dependency, while other methods might introduce many variables not able to be fully controlled that would possibly alter the final results [67].

In the following section, the experimental setup is described, followed by the theory of 1st order reaction (Langmuir-Hinshelwood theory). Finally, the results of the experiments are presented and corresponding derivation through the theory is also illustrated.

5.1 Experimental Setup and Procedures

5.1.1 Reactor Chamber Setup

To determine the photocatalytic activity for $Ce_xZr_{1-x}O_2$ nanoparticles, a reactor was designed and built by our lab, as shown in Figure 5-1. The inner wall of the chamber was covered by UV absorptive sheets. Those protective materials aimed to reduce the scattered radiation during the experiment. As temperature was also a factor which could contribute to the results of photocatalytic reaction, a 5 W electric fan was placed on top of the chamber for convective heat transport in order to keep a constant temperature in the chamber. With this set-up the temperature in the reaction vials was monitored to be 26.0 ± 0.5 °C after 2 °C increase in the first 20 minutes. To initiate the reaction, three 8 W UV lamps were used as the irradiative light sources. Depending on the experiment, lamps with peak wavelength at 302nm or 365nm were used for the test. Samples were kept in transparent glass vials 20 cm below the lamps. The light intensity received by samples in this configuration was determined to be approximately 15 W/m^2 .

5.1.2 Dye Selection

The photocatalytic efficiency of $Ce_xZr_{1-x}O_2$ nanoparticles was tested by a series of experiments using a dye degradation method. Brilliant Procion® Red MX-5B ($C_{19}H_{13}Cl_2N_6Na_2O_7S_2$) with its chemical structure shown in Figure 5-2 was chosen for our experiments [68]. This dye has a three-stage degradation mechanism in response to the presence of hydroxyl groups. In the 1st stage, the most active bonds, including C-N bond and C-S bond are hydroxylated. After that, groups linked to the triazine ring are replaced by a hydroxyl group to produce cyanuric acid. Finally, further oxidation of the yields from previous steps would form CO_2 , water and minerals to complete the reaction. The intermediate compounds in the reaction are summarized in Table 5-1, according to reference [69]. More detailed degradation mechanism of the dye has been developed by several groups like H. Lachheb et al. [66] and C.M. So et al. [70], and will not be covered in this thesis.

The use of Procion® Red MX-5B could mainly be attributed to its moderate rate of degradation under common conditions [71]. It is a critical issue for photocatalysis since too fast a reaction often causes difficulty in system stabilization and the parameters for reaction are hard to control, while in slow reaction water evaporation would yield uncertainties in aqueous systems. The absorption peak for Procion® Red MX-5B lies in between 510 nm to 540 nm, and is experimentally determined to be 533 nm, as shown in Figure 5-3.

5.1.3 Procedures

In the experiment, Procion® Red MX-5B was diluted to 5 ppm and mixed with 0.75 mM $Ce_xZr_{1-x}O_2$ nanoparticle suspensions. 0.05 μ M potassium phosphate buffer was added into the suspension to maintain the pH value during the whole reaction. The UV lamps were turned on 30 minutes ahead to allow the stabilization of light intensity. A series of samples were prepared and fully mixed before being placed in the chamber for reaction. The chamber was isolated from

outer light sources and the samples are irradiated by UV light. Portions of the samples were obtained every 40 minutes from the reaction vials and titrated in 1.5 ml plastic cuvettes. The residual dye concentration in the cuvettes was monitored by UV/VIS spectrometer as a function of peak absorbance at 533 nm. The total reaction time was 360 minutes and reaction constant is calculated based on Langmuir-Hinshelwood theory. Since nanosize particles were well-dispersed and also capable of scattering light, control samples with only $Ce_xZr_{1-x}O_2$ nanoparticles in a concentration equal to the ongoing experimental sets were prepared as reference to determine the absorbance solely contributed by the remaining dye.

For comparison of photocatalytic activity between currently commercialized photocatalyst and the particles synthesized in our lab, Aeroxide® TiO₂ P25 from Evonik Industries was used. It is one of the most powerful commercial photocatalysis systems [72], and is considered an ideal material to compare the photocatalytic efficiencies. As an important parameter for photocatalytic reactions, the specific surface area for Aeroxide® TiO₂ P25 is reported to be 50±15 m²/g from Evonik Industries and was directly used for calculation. Additionally, a parallel experiment employing NanoActive Cerium Oxide from NanoScale Corporation was also conducted as comparison between our particles and commercial nanosize ceria particles. The specific surface area was reported to be >50 m²/g and was also directly used.

5.2 Theory for Photocatalytic Degradation Reaction

Langmuir-Hinshelwood theory is the most commonly used kinetic model for describing photocatalytic behaviors [67, 68, 73, 74]. In this model, it is assumed that the overall reaction rate depends on the adsorption of dye molecules on catalytic particles as well as the reaction rates. The photocatalytic oxidation in Langmuir-Hinshelwood theory is given by equation 5-1:

$$r = -\frac{dC_t}{dt} = -\frac{kKC_t}{1 + KC_t} \quad (5-1)$$

or

$$\frac{1}{r} = \frac{1}{k} + \frac{1}{kKC_t} \quad (5-2)$$

where r is the reaction rate, k is the overall rate constant, C_t is the dye concentration, and K is the adsorption coefficient [74]. The solution for Equation 5-1 is given out by Equation 5-3:

$$\ln\left(\frac{C_t}{C_0}\right) + K(C_t - C_0) = -kKt \quad (5-3)$$

where C_0 is the initial concentration of the dye.

Equation 5-3 could be solved for t by a series of experimental data with discrete value of C_t from C_0 to 0. It is a nonlinear solution but when C_0 approaches 0,

$$\ln\left(\frac{C_t}{C_0}\right) \gg K(C_t - C_0) \quad (5-4)$$

and a pseudo first-order solution could be assumed, as shown in Equation 5-5:

$$r = -\frac{dC_t}{dt} = k'C_t = kKC_t \quad (5-5)$$

where k' is the overall reaction constant in the unit of time^{-1} , and the equation could be integrated as:

$$\ln\left(\frac{C_t}{C_0}\right) = -kKt = -k't \quad (5-6)$$

or

$$C_t = C_0 e^{-k't} \quad (5-7)$$

in which a clearly exponential decay could be expected.

However, the photocatalytic reactions are also affected by many other parameters. For reactions conducted under different experimental conditions, variations in other factors, such as

catalysts load, pH, and light intensity will also be taken into consideration. Additional terms must be added into the solution for the general Langmuir-Hinshelwood model to represent these variations.

Additionally, in the Langmuir-Hinshelwood model the reaction is assumed to be a single-step reaction, which is not true for the case in reality. However, for the simplification of analysis, it is assumed that there is a rate-determining step within all the reactions and k' represents the rate constant of this slowest one.

5.3 Results and Discussion

5.3.1 Photocatalysis of $Ce_xZr_{1-x}O_2$ nanoparticles under 302 nm UV irradiation

This set of experiments aimed to investigate the photocatalytic efficiency of $Ce_xZr_{1-x}O_2$ nanoparticles under the agitation of UV-B (302 nm) lights, which far exceeded the bandgap 3.40 eV~4.55 eV of target nanoparticles. The experiments were conducted with a same concentration based on cerium/zirconium ions. Samples were prepared according to the protocols described in section 5.1.3. However, for the commercial ceria particle from NanoScale Corporation, the concentration was 2 mM instead of 0.75 mM as no noticeable photocatalytic activity had been observed for the system with that concentration. Suspensions with higher concentrations were also tested but due to severe agglomeration and sedimentation, their activity degraded again.

Figure 5-4 showed the photocatalytic degradation results for Procion® Red MX-5B dye under 302 nm UV light radiation as a function of time. Y axis denoted the residual dye compared to its original concentration. The residual concentration of the dye was evaluated by UV/VIS spectroscopy with Beer-Lambert's Law (Equation 4-4).

The upper most curve showed the dye performance under 302nm UV radiation when there was no photocatalysts present. It was worthy to note that the water itself could not generated sufficient free radical groups to cause the degradation of the dye even under such harsh

exposures for as long as 6 hours. It was crucial since external contributions to photocatalysis could cause difficulty in evaluating the activity among synthesized nanoparticles.

Besides the “no particle” control sample, photocatalytic activity had been observed with the presence of different particles. Proved to be a non-efficient photocatalyst, ZrO_2 particles displayed some catalytic activity under our experimental condition but were insignificant. Surprisingly, NanoActive ceria from NanoScale Corporation, performed second-worst in all sets of experiments with the presence of particles. Its photocatalytic activity barely exceeded that from the synthesized zirconia particles. Such a result might either be explained by the higher concentration in the experimental suspensions or the inadequate surface area due to agglomeration. The drastic drop observed for both the zirconia and NanoActive ceria samples were most probably caused by experimental errors.

Regarding the catalytic results for $Ce_xZr_{1-x}O_2$ nanoparticles, better catalytic activity had been displayed than zirconia and NanoActive ceria samples. Interestingly, a noticeable trend could also be found that compounds with higher zirconium composition showed a better photocatalytic activity. The reasons for the tendency was largely unknown but the speculation was that there might be more $[Ce^{3+}]$ in these compounds. This issue will be discussed in a latter part of the chapter.

In the bottom of the diagram, the Aeroxide® TiO_2 P25, a currently commercialized photocatalyst, showed the best catalytic activity within all the experimental sets. Also, in this series of experiment, the Aeroxide® TiO_2 P25 was the only photocatalyst be able to degrade the entire dye in the suspension.

5.3.2 Photocatalysis of $Ce_xZr_{1-x}O_2$ nanoparticles under 365 nm UV irradiation

This series of experiment was designed and run to evaluate the performance of $Ce_xZr_{1-x}O_2$ nanoparticles under the irradiation of 365 nm UV light. 365 nm lies within UV-A region and

constructed portion of the sunlight in routine life. It was an ideal wavelength for testing the nanoparticles if they were feasible for outdoor uses. The samples were also prepared according to the protocols in 5.1.3 except for NanoActive ceria, which was prepared in a concentration of 2 mM as in the 302 nm UV irradiation test.

The degradation results for the dye were presented in Figure 5-5. As had been expected, water itself could not cause dye degradation under 365 nm UV radiations. Also, except for the Aeroxide® TiO₂ P25 commercialized photocatalyst, all the other experimental sets did not exhibit any photocatalytic activity under such condition. The lack of photocatalysis in synthesized Ce_xZr_{1-x}O₂ nanoparticles could be explained by the bandgap value achieved in section 4.5.2. Even the ceria with lowest bandgap 3.58 eV among all the Ce_xZr_{1-x}O₂ nanoparticles would require a light source with λ as low as 348 nm to generate excitons. Thus it was reasonable to conclude the synthesized Ce_xZr_{1-x}O₂ nanoparticles have no photocatalytic activity under such wavelength. On the other hand, the catalytic activity results also proved the correctness of the calculation in the previous chapter.

For the two comparison sets, Aeroxide® TiO₂ P25 and NanoActive ceria, Aeroxide® TiO₂ P25 maintained to be most photoactive but its activity was not as good as that under the irradiation under 302 nm UV light. Interestingly, though the photonic energy of impinging light (3.40 eV) was theoretically sufficient to overcome the bandgap of NanoActive ceria samples, they still did not exhibit any photocatalytic activity. The drastic drop during the first 40 minutes might rather be caused by experimental error than photocatalytic response.

5.3.3 Rate Constant Calculation and Implications

As has been discussed above, photocatalytic reactions generally follow a first-order reaction model, and could be described by Langmuir-Hinshelwood model.

By applying Equation 5-6 and fitting the degradation curves, the calculated rate constant for $Ce_xZr_{1-x}O_2$ nanoparticles were presented in Table 5-2. Contrast samples were also included in the table. As photocatalytic activity was a surface-sensitive property, the final calculation of rate constants were normalized to the surface area presented in Table 5-2.

The table clearly showed a photocatalytic activity from $Ce_xZr_{1-x}O_2$ nanoparticles 1~2 orders weaker than that of commercial Aeroxide[®] TiO₂ P25 from Evonik Industries under 302 nm UV radiation. The low catalytic activity for the synthesized particles was a good implication for their bio medical applications especially under sunlight exposures, which has portions in the UV range.

As has been mentioned above, another interesting trend displayed in the rate constant was the increase in photocatalytic activities with increase in zirconium content in $Ce_xZr_{1-x}O_2$ nanoparticles. A six-fold raise was achieved by $Ce_{0.2}Zr_{0.8}O_2$ particles over pure ceria. The mechanism for the zirconium content in increasing the photocatalytic activity was largely unknown. However, analogic trends had been discovered in the superoxide scavenging activity of these nanoparticles. Also, high temperature oxygen storage property of ceria-zirconia solid solutions displayed a similar tendency. With both of the two above mentioned properties depending largely on the $[Ce^{3+}]/[Ce^{4+}]$ ratio in solid solution lattice, suspicion was raised that the presence of Ce^{3+} site might also play an important role in the photocatalysis process, e.g. retarding the recombination of excitons. Yet more research into it will still be needed for fully understanding of the whole mechanism.

5.4 Summary

In this chapter a series of experiments were performed to evaluate the photocatalytic activity of synthesized $Ce_xZr_{1-x}O_2$ nanoparticles. The goal was achieved by the degradation of Procion[®] Red MX-5B dye. Several control samples were made to eliminate the external factors

that might affect the final results. Catalytic rate constant solely contributed by the activity of synthesized particles were obtained. To compare the activity of particles from our lab and those commercialized ones, Aeroxide® TiO₂ P25 from Evonik Industries and NanoActive Cerium Oxide from NanoScale Corporation were used for parallel experiments. By carefully analyzing and comparing the results, following conclusions were confirmed:

- Ce_xZr_{1-x}O₂ nanoparticles displayed photocatalytic activity under the radiation of 302 nm UV light. Their performance exceeded that of NanoActive Cerium Oxide but was 1~2 orders lower to that of Aeroxide® TiO₂ P25, a commercialized photocatalyst.
- The photocatalytic activity of Ce_xZr_{1-x}O₂ nanoparticles increased as the zirconium component increased under 302 nm UV irradiation.
- Ce_xZr_{1-x}O₂ nanoparticles did not display any photocatalytic activity under 365 nm UV light radiation.
- The behavior of photocatalysis of Ce_xZr_{1-x}O₂ nanoparticles resembled their performance in free radical scavenging and oxygen storage capacity. This phenomenon indicated that there might be some common mechanisms contributing to each of their applications.

Table 5-1. Photocatalytic reaction intermediates summarized for different stages ^[69]

Stage	Photocatalytic Reaction Intermediates
	p-Hydroxy-phenyl-3-hydroxy-propanedioic acid, 3-Hydroxy-
1	benzeneacetic acid, 2-Hydroxy-benzoic acid, p-Hydroxy-cinnamic acid 1,2-Benzenedicarboxylic acid
2	Cyanuric acid, 1-Propene-1,2,3-tricarboxylic acid, Propanedioic acid Propanoic acid, Malic acid, Butenedioic acid, Oxalic acid, Acetic acid
3	CO ₂ and H ₂ O, Minerals (sulfuric compounds)

Table 5-2. Normalized rate constants of photocatalytic degradation of Procion Red MX-5B for the synthesized Ce_xZr_{1-x}O₂ nanoparticles under 302 nm and 365 nm UV illumination

Sample	Rate const. for 302 nm UV light radiated sample ($\times 10^{-5} \text{m}^{-2} \text{s}^{-1}$)	Rate const. for 365 nm UV light radiated sample ($\times 10^{-5} \text{m}^{-2} \text{s}^{-1}$)
Blank	0	0
Aeroxide® TiO ₂ P25	610±80	370±80
CeO ₂	7±2	0
Ce _{0.8} Zr _{0.2} O ₂	19±3	0
Ce _{0.7} Zr _{0.3} O ₂	18±3	0
Ce _{0.6} Zr _{0.4} O ₂	20±3	0
Ce _{0.4} Zr _{0.6} O ₂	32±3	0
Ce _{0.2} Zr _{0.8} O ₂	44±5	0

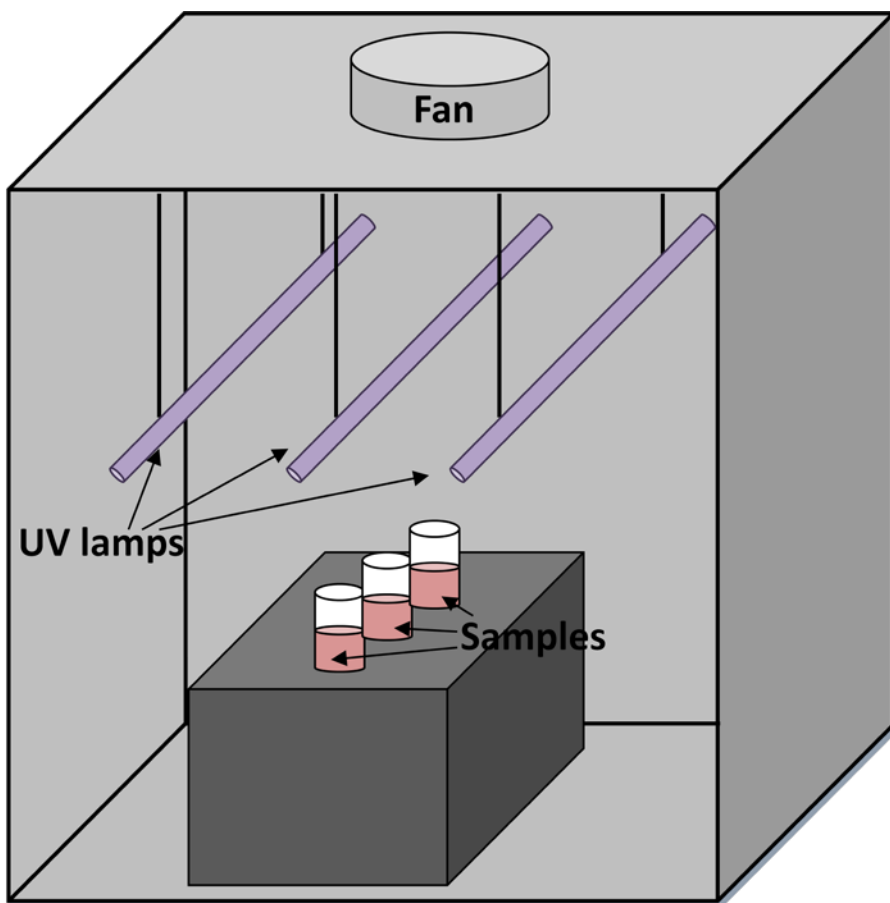


Figure 5-1. Sketch of the reactor chamber

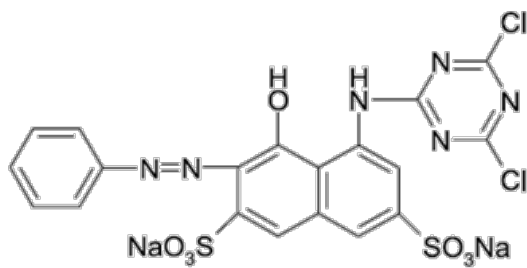


Figure 5-2. The chemical structure of Procion® Red MX-5B ^[68]

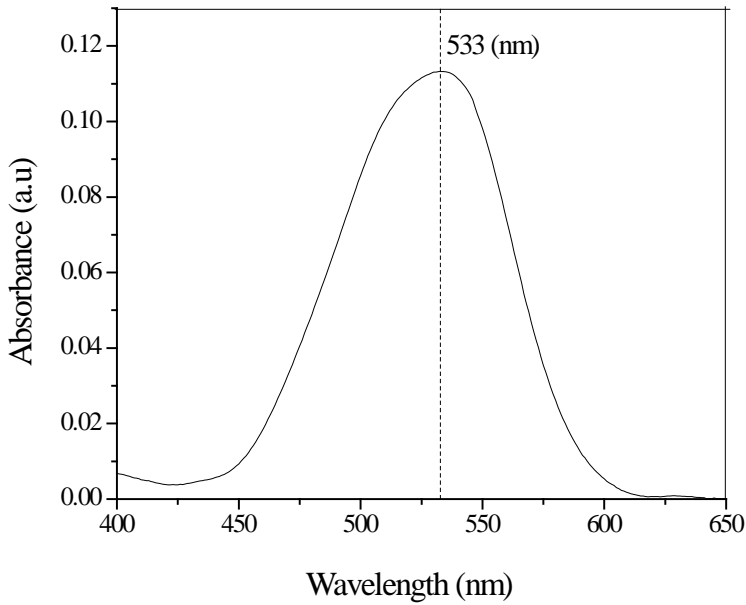


Figure 5-3. The absorption spectrum for 5 ppm solution of the Procion® Red MX-5B dye

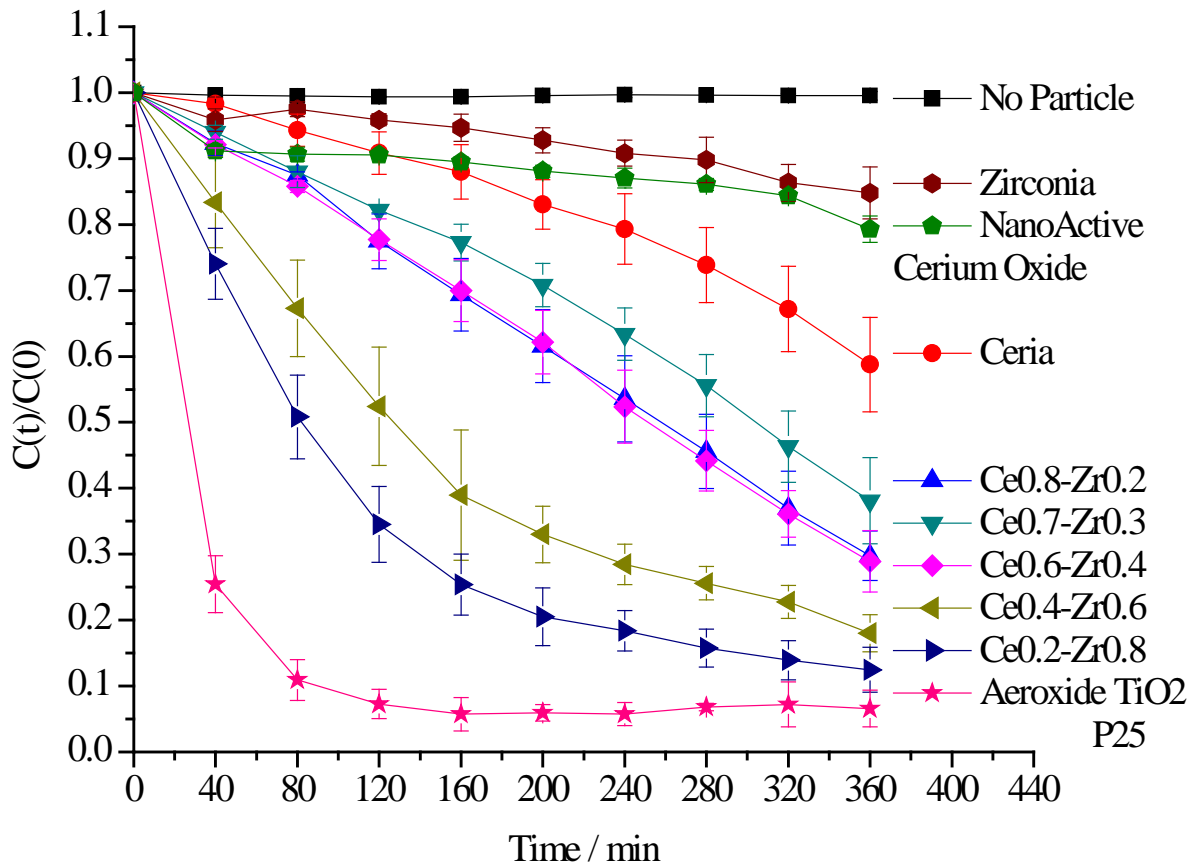


Figure 5-4. Time dependence of normalized residual dye concentration for irradiation with 302 nm UV light

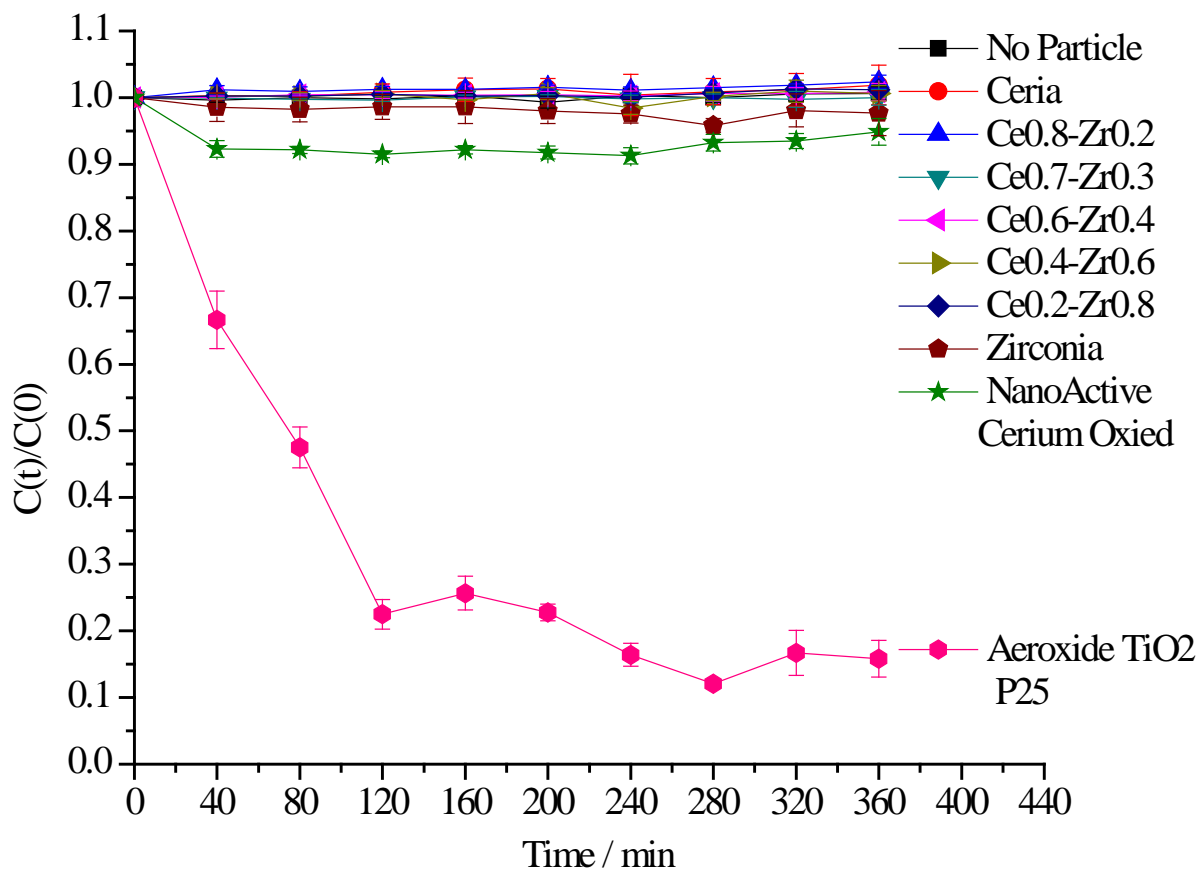


Figure 5-5. Time dependence of normalized residual dye concentration for irradiation with 365 nm UV light

CHAPTER 6 IMPLICATIONS AND CONCLUSIONS

6.1 Implications and Future Work

$Ce_xZr_{1-x}O_2$ nanoparticles are found to possess the photocatalytic activity to degrade the Procion® Red MX-5B azo dye. The catalytic activity of these nanoparticles, though not comparable to that of the current commercialized photocatalyst Aeroxide® TiO₂ P25, has displayed an increasing trend when the content of zirconium increases. Proved to be effective in increasing the efficiency of CeO₂ as three-way-catalyst [40] and free radical scavengers [13], zirconium substitution also seems to be beneficial in enhancing CeO₂'s photocatalytic activity. Though the mechanism for the tendency is not fully investigated, analogue trends imply a common mechanism, or at least shared components for those different applications. Figure 6-1 shows the equilibrium single cell structure for fluorite $Ce_xZr_{1-x}O_2$ compound [40].

It is suggested that the introduction of zirconium into CeO₂ lattice would assist the generation of oxygen vacancies due to the difference in ionic radius between Zr⁴⁺ and Ce⁴⁺ ions. The increase in oxygen vacancies in the lattice will in turn give rise to the ratio of [Ce³⁺] to [Ce⁴⁺]. XPS data from section 4.4.4 also confirm the increase of oxygen content in the same set of particles after the photocatalytic experiment. The environmental oxygen species are possibly incorporated into the lattice during the photocatalysis reactions.

According to Y.Y. Tsai's efforts on the biomedical application of $Ce_xZr_{1-x}O_2$ nanoparticles [13], the reaction pathway for $Ce_xZr_{1-x}O_2$ nanoparticles' free radical scavenging properties is summarized in Figure 6-2. It should be noticed that there are many species also existing in the redox reactions for semiconductor photocatalysis. Thus the implication is that equilibrium oxygen vacancies also play an important role in the photocatalysis of $Ce_xZr_{1-x}O_2$ nanoparticles,

and the photocatalysis and free radical scavenging properties might be counter-reactions for these nanosize particles.

However, the speculation made above is largely not proved and more research would be necessary to investigate into the mechanism between their photocatalytic activity and free radical scavenging properties. Future works including the tests of $\text{Ce}_x\text{Zr}_{1-x}\text{O}_2$ nanoparticles in the presence of both UV light irradiation and pre-generated reactive oxygen species might help to generate a better understanding of these nanoparticles.

6.2 Conclusions

According to experiments and discussions in previous chapters, the following conclusion for this thesis could be summarized:

- $\text{Ce}_x\text{Zr}_{1-x}\text{O}_2$ nanoparticles synthesized through reverse micelle method. Specific surface area of $109\pm 20 \text{ m}^2/\text{g}$ has been calculated for these nanoparticles from their dynamic light scattering diameters.
- The synthesized $\text{Ce}_x\text{Zr}_{1-x}\text{O}_2$ nanoparticles display a well defined crystalline state.
- Zirconium substitution induces the generation of oxygen vacancies and Ce^{3+} sites in the CeO_2 lattice.
- UV irradiation promotes the incorporation of environmental oxygen species into the CeO_2 lattice.
- These nanosize particles displayed an absorption band in the UV region. Their bandgaps were larger than bulk materials due to the quantum confinement effect, which affects their photocatalytic activities.
- The catalytic activity of synthesized nanoparticles was 1~2 orders lower than commercialized Aeroxide® TiO_2 P25 photocatalyst, but better than NanoActive Cerium Oxide from NanoScale Corporation, under 302 nm UV light illumination. No measurable activity has been observed for $\text{Ce}_x\text{Zr}_{1-x}\text{O}_2$ nanoparticles under 365 nm UV light. Thus their photocatalytic activity under sunlight should be insignificant.
- Zirconium substitution enhances the photocatalytic activity of ceria nanoparticles. As there are analogous trends in the reaction rates of free radical scavenging and the oxygen storage capacity of cerium-zirconium dioxide solid solutions, a common mechanism explaining both is hypothesized.

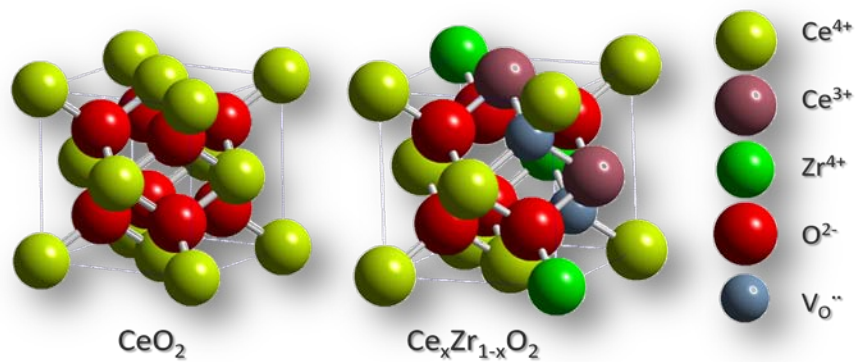


Figure 6-1. Schematic structure for CeO_2 and $\text{Ce}_x\text{Zr}_{1-x}\text{O}_2$ crystals.

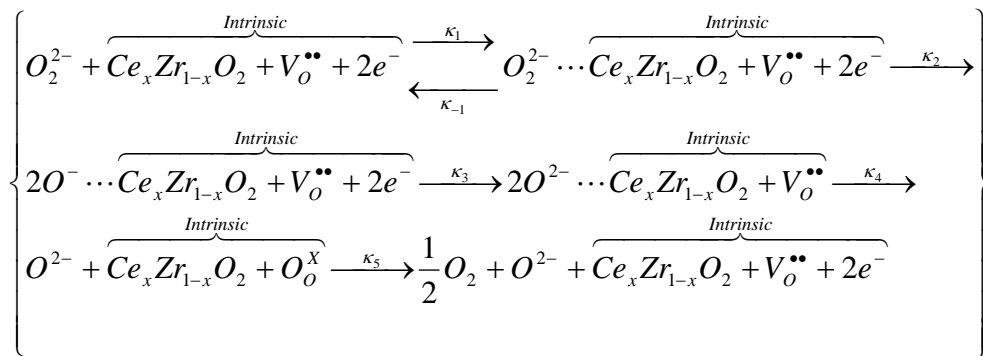


Figure 6-2. The reaction pathway for $\text{Ce}_x\text{Zr}_{1-x}\text{O}_2$ nanoparticles free radical scavengers ^[13]

LIST OF REFERENCES

- [1] Telek, G.; Scoazec, J. Y.; Chariot, J.; Ducroc, R.; Feldmann, G.; Roze, C. Cerium-based histochemical demonstration of oxidative stress in taurocholate-induced acute pancreatitis in rats: A confocal laser scanning microscopic study. *Journal of Histochemistry & Cytochemistry* **47**:1201-1212; 1999.
- [2] Trovarelli, A. *Catalysis by Ceria and Related Materials*. London: Imperial College Press; 2005.
- [3] Dalslet, B.; Blennow, P.; Hendriksen, P. V.; Bonanos, N.; Lybye, D.; Mogensen, M. Assessment of doped ceria as electrolyte. *Journal of Solid State Electrochemistry* **10**:547-561; 2006.
- [4] Eguchi, K. Ceramic materials containing rare earth oxides for solid oxide fuel cell. *Journal of Alloys and Compounds* **250**:486-491; 1997.
- [5] Jasinski, P.; Suzuki, T.; Anderson, H. U. Nanocrystalline undoped ceria oxygen sensor. *Sensors and Actuators B-Chemical* **95**:73-77; 2003.
- [6] Descorme, C.; Madier, Y.; Duprez, D. Infrared study of oxygen adsorption and activation on cerium-zirconium mixed oxides. *Journal of Catalysis* **196**:167-173; 2000.
- [7] Bamwenda, G. R.; Arakawa, H. Cerium dioxide as a photocatalyst for water decomposition to O₂ in the presence of Ce-aq(4+) and Fe-aq(3+) species. *Journal of Molecular Catalysis a-Chemical* **161**:105-113; 2000.
- [8] Das, M.; Patil, S.; Bhargava, N.; Kang, J. F.; Riedel, L. M.; Seal, S.; Hickman, J. J. Auto-catalytic ceria nanoparticles offer neuroprotection to adult rat spinal cord neurons. *Biomaterials* **28**:1918-1925; 2007.
- [9] Tsai, Y. Y.; Oca-Cossio, J.; Agering, K.; Simpson, N. E.; Atkinson, M. A.; Wasserfall, C. H.; Constantinidis, I.; Sigmund, W. Novel synthesis of cerium oxide nanoparticles for free radical scavenging. *Nanomedicine* **2**:325-332; 2007.
- [10] Duwez, P.; Odell, F. Phase Relationships in the System Zirconia-Ceria. *Journal of the American Ceramic Society* **33**:274-283; 1950.
- [11] Diaz, E.; de Rivas, B.; Lopez-Fonseca, R.; Ordonez, S.; Gutierrez-Ortiz, J. I. Characterization of ceria-zirconia mixed oxides as catalysts for the combustion of volatile organic compounds using inverse gas chromatography. *Journal of Chromatography A* **1116**:230-239; 2006.
- [12] Reddy, B. M.; Bharali, P.; Thrimurthulu, G.; Saikia, P.; Katta, L.; Park, S. E. Catalytic efficiency of ceria-zirconia and ceria-hafnia nanocomposite oxides for soot oxidation. *Catalysis Letters* **123**:327-333; 2008.

- [13] Tsai, Y. Y.; Oca-Cossio, J.; Lin, S. M.; Woan, K.; Yu, P. C.; Sigmund, W. Reactive oxygen species scavenging properties of ZrO₂-CeO₂ solid solution nanoparticles. *Nanomedicine* **3**:637-645; 2008.
- [14] Kaneko, M.; Okura, I. *Photocatalysis: Science and Technology*. Springer; 2003.
- [15] Fujishim, A.; Honda, K. I. Studies on Photosensitive Electrode Reaction .2. Evidence of Photosensitized Electrolytic Oxidation on TiO₂ Electrode from Ph Change of Electrolyte Solution. *Kog Kagaku Zasshi* **74**:355-&; 1971.
- [16] Fujishima, A.; Honda, K. Electrochemical Photolysis of Water at a Semiconductor Electrode. *Nature* **238**:37-38; 1972.
- [17] Fujishima, A.; Kohayakawa, K.; Honda, K. Hydrogen Production under Sunlight with an Electrochemical Photocell. *Journal of the Electrochemical Society* **122**:1487-1489; 1975.
- [18] Jaegermann, W. The semiconductor/electrolyte interface: a surface science approach. In: R.E. White, B. E. C., J. O'M. Bockris, ed. *Modern Aspects of Electrochemistry*. New York: Plenum Press; 1996: 1-185.
- [19] Fox, M. A.; Dulay, M. T. Acceleration of secondary dark reactions of intermediates derived from adsorbed dyes on irradiated TiO₂ powders. *Journal of Photochemistry and Photobiology a-Chemistry* **98**:91-101; 1996.
- [20] Mills, A.; LeHunte, S. An overview of semiconductor photocatalysis. *Journal of Photochemistry and Photobiology a-Chemistry* **108**:1-35; 1997.
- [21] Fujishima, A.; Rao, T. N.; Tryk, D. A. Titanium dioxide photocatalysis *Journal of Photochemistry and Photobiology C: Photochemistry Reviews* **1**:1-21; 2000.
- [22] Martin, S. T.; Herrmann, H.; Hoffmann, M. R. Time-Resolved Microwave Conductivity .2. Quantum-Sized TiO₂ and the Effect of Adsorbates and Light-Intensity on Charge-Carrier Dynamics. *Journal of the Chemical Society-Faraday Transactions* **90**:3323-3330; 1994.
- [23] Martin, S. T.; Herrmann, H.; Choi, W. Y.; Hoffmann, M. R. Time-Resolved Microwave Conductivity .1. TiO₂ Photoreactivity and Size Quantization. *Journal of the Chemical Society-Faraday Transactions* **90**:3315-3322; 1994.
- [24] Hoffmann, M. R.; Martin, S. T.; Choi, W. Y.; Bahnemann, D. W. Environmental Applications of Semiconductor Photocatalysis. *Chemical Reviews* **95**:69-96; 1995.
- [25] Beydoun, D.; Amal, R.; Low, G.; Mcevoy, S. Role of Nanoparticles in Photocatalysis. *Journal of Nanoparticle Research* **1**:439-458; 1999.

- [26] Levy, B. Photochemistry of Nanostructured Materials for Energy Applications. *Journal of Electroceramics* **1**:239-272; 1997.
- [27] Kamat, P. V.; Meisel, D. Nanoscience opportunities in environmental remediation. *Comptes Rendus Chimie* **6**:999-1007; 2003.
- [28] Frohlich, H. Dielectric breakdown in ionic crystals. *Physical Review* **56**:349-352; 1939.
- [29] Frohlich, H. Theory of electrical breakdown in ionic crystals. II. *Proceedings of the Royal Society of London Series a-Mathematical and Physical Sciences* **172**:0094-0106; 1939.
- [30] Frohlich, H. Theory of electrical breakdown in ionic crystals. *Proceedings of the Royal Society of London Series a-Mathematical and Physical Sciences* **160**:0230-0241; 1937.
- [31] Yoffe, A. D. Low-Dimensional Systems - Quantum-Size Effects and Electronic-Properties of Semiconductor Microcrystallites (Zero-Dimensional Systems) and Some Quasi-2-Dimensional Systems. *Advances in Physics* **42**:173-266; 1993.
- [32] Gratzel, M. *Heterogeneous Photochemical Electron Transfer*. Boca Raton: CRC Press Inc.; 1989.
- [33] Wise, F. W. Lead salt quantum dots: The limit of strong quantum confinement. *Accounts of Chemical Research* **33**:773-780; 2000.
- [34] Miao, J. J.; Wang, H.; Li, Y. R.; Zhu, J. M.; Zhu, J. J. Ultrasonic-induced synthesis of CeO₂ nanotubes. *Journal of Crystal Growth* **281**:525-529; 2005.
- [35] Rzigalinski, B. A. Nanoparticles and cell longevity. *Technology in Cancer Research & Treatment* **4**:651-659; 2005.
- [36] Rzigalinski, B. A.; Meehan, K.; Davis, R. M.; Xu, Y.; Miles, W. C.; Cohen, C. A. Radical nanomedicine. *Nanomedicine* **1**:399-412; 2006.
- [37] Schubert, D.; Dargusch, R.; Raitano, J.; Chan, S. W. Cerium and yttrium oxide nanoparticles are neuroprotective. *Biochemical and Biophysical Research Communications* **342**:86-91; 2006.
- [38] Tarnuzzer, R. W.; Colon, J.; Patil, S.; Seal, S. Vacancy engineered ceria nanostructures for protection from radiation-induced cellular damage. *Nano Letters* **5**:2573-2577; 2005.
- [39] Ormerod, R. M. Solid oxide fuel cells. *Chemical Society Reviews* **32**:17-28; 2003.
- [40] Troverelli, A. *Catalysis by Ceria and Related Materials*. London: World Scientific Publishing Company; 2002.

- [41] Yashima, M.; Morimoto, K.; Ishizawa, N.; Yoshimura, M. Diffusionless Tetragonal Cubic Transformation Temperature in Zirconia Ceria Solid-Solutions. *Journal of the American Ceramic Society* **76**:2865-2868; 1993.
- [42] Yashima, M.; Morimoto, K.; Ishizawa, N.; Yoshimura, M. Zirconia Ceria Solid-Solution Synthesis and the Temperature Time Transformation Diagram for the 1/1 Composition. *Journal of the American Ceramic Society* **76**:1745-1750; 1993.
- [43] Vidal, H.; Kaspar, J.; Pijolat, M.; Colon, G.; Bernal, S.; Cordon, A.; Perrichon, V.; Fally, F. Redox behavior of CeO₂-ZrO₂ mixed oxides - II. Influence of redox treatments on low surface area catalysts. *Applied Catalysis B-Environmental* **30**:75-85; 2001.
- [44] Vidal, H.; Kaspar, J.; Pijolat, M.; Colon, G.; Bernal, S.; Cordon, A.; Perrichon, V.; Fally, F. Redox behavior of CeO₂-ZrO₂ mixed oxides I. Influence of redox treatments on high surface area catalysts. *Applied Catalysis B-Environmental* **27**:49-63; 2000.
- [45] Sasaki, T.; Ukyo, Y.; Kuroda, K.; Arai, S.; Saka, H. Microstructural investigation of ceria-zirconia solid solution with oxygen vacancies. *Journal of Electron Microscopy* **52**:309-312; 2003.
- [46] Zhang, J.; Sun, L. D.; Liao, C. S.; Yan, C. H. Size control and photoluminescence enhancement of CdS nanoparticles prepared via reverse micelle method. *Solid State Communications* **124**:45-48; 2002.
- [47] Steigerwald, M. L.; Alivisatos, A. P.; Gibson, J. M.; Harris, T. D.; Kortan, R.; Muller, A. J.; Thayer, A. M.; Duncan, T. M.; Douglass, D. C.; Brus, L. E. Surface Derivatization and Isolation of Semiconductor Cluster Molecules. *Journal of the American Chemical Society* **110**:3046-3050; 1988.
- [48] Modes, S.; Lianos, P. Luminescence Probe Study of the Conditions Affecting Colloidal Semiconductor Growth in Reverse Micelles and Water-in-Oil Microemulsions. *Journal of Physical Chemistry* **93**:5854-5859; 1989.
- [49] Nakanishi, T.; Ohtani, B.; Uosaki, K. Construction of semiconductor nanoparticle layers on gold by self-assembly technique. *Japanese Journal of Applied Physics Part 1-Regular Papers Short Notes & Review Papers* **36**:4053-4056; 1997.
- [50] Kim, D.; Miyamoto, M.; Mishima, T.; Nakayama, M. Strong enhancement of band-edge photoluminescence in CdS quantum dots prepared by a reverse-micelle method. *Journal of Applied Physics* **98**; 2005.
- [51] Zhang, D. B.; Qi, L. M.; Cheng, H. M.; Ma, J. M. Synthesis of crystalline nanosized titanium dioxide via a reverse micelle method at room temperature. *Chinese Chemical Letters* **14**:100-103; 2003.

- [52] Yin, Y.; Alivisatos, A. P. Colloidal nanocrystal synthesis and the organic-inorganic interface. *Nature* **437**:664-670; 2005.
- [53] Seo, S. H.; Chung, C. W.; Chang, H. Y. Review of heating mechanism in inductively coupled plasma. *Surface & Coatings Technology* **131**:1-11; 2000.
- [54] Brenner, I. B.; Taylor, H. E. A Critical-Review of Inductively Coupled Plasma-Mass Spectrometry for Geoanalysis, Geochemistry, and Hydrology .1. Analytical Performance. *Critical Reviews in Analytical Chemistry* **23**:355-367; 1992.
- [55] Evans, E. H.; Giglio, J. J. Interferences in Inductively Coupled Plasma Mass-Spectrometry - a Review. *Journal of Analytical Atomic Spectrometry* **8**:1-18; 1993.
- [56] Matusiewicz, H. Thermal Vaporization for Inductively Coupled Plasma Optical-Emission Spectrometry - a Review. *Journal of Analytical Atomic Spectrometry* **1**:171-184; 1986.
- [57] Berne, B. J.; Pecora, R. *Dynamic Light Scattering: With Applications to Chemistry, Biology, and Physics*. New York: Dover Publications, Inc.; 2000.
- [58] Stein, R. S.; Rowell, R. L. *The Scattering of Light and Other Electromagnetic Radiation*. New York: Academic Press; 1969.
- [59] Schroder, D. K. *Semiconductor Material and Device Characterization*. New York: Wiley-Interscience/IEEE; 2006.
- [60] Williams, D. B.; Carter, C. B. *Transmission electron microscopy: a textbook for materials science*. New York: Springer; 1996.
- [61] Crist, B. V. *Handbooks of Monochromatic XPS Spectra*. Mountain View, CA: XPS International LLC; 2004.
- [62] Horst Ebel, R. S., Maria F. Ebel and Wolfgang S.M. Werner. Comparison of three universal curves for the escape probability of X-ray excited electrons - I. Theory. *Advances in X-ray Analysis* **44**:380-385; 2001.
- [63] Dakhel, A. A. Correlated transport and optical phenomena in Ga-doped CdO films. *Solar Energy* **82**:513-519; 2008.
- [64] Joshi, G. P.; Saxena, N. S.; Mangal, R.; Mishra, A.; Sharma, T. P. Band gap determination of Ni-Zn ferrites. *Bulletin of Materials Science* **26**:387-389; 2003.
- [65] Doushita, K.; Kawahara, T. Evaluation of photocatalytic activity by dye decomposition. *Journal of Sol-Gel Science and Technology* **22**:91-98; 2001.
- [66] Lachheb, H.; Puzenat, E.; Houas, A.; Ksibi, M.; Elaloui, E.; Guillard, C.; Herrmann, J. M. Photocatalytic degradation of various types of dyes (Alizarin S, Crocein Orange G,

- Methyl Red, Congo Red, Methylene Blue) in water by UV-irradiated titania. *Applied Catalysis B-Environmental* **39**:75-90; 2002.
- [67] Hu, C.; Yu, J. C.; Hao, Z.; Wong, P. K. Effects of acidity and inorganic ions on the photocatalytic degradation of different azo dyes. *Applied Catalysis B-Environmental* **46**:35-47; 2003.
- [68] Galindo, C.; Jacques, P.; Kalt, A. Photodegradation of the aminoazobenzene acid orange 52 by three advanced oxidation processes: UV/H₂O₂ UV/TiO₂ and VIS/TiO₂ - Comparative mechanistic and kinetic investigations. *Journal of Photochemistry and Photobiology a-Chemistry* **130**:35-47; 2000.
- [69] Hu, C.; Yu, J. C.; Hao, Z. P.; Wong, P. K. Photocatalytic degradation of triazine-containing azo dyes in aqueous TiO₂ suspensions. *Applied Catalysis B-Environmental* **42**:47-55; 2003.
- [70] So, C. M.; Cheng, M. Y.; Yu, J. C.; Wong, P. K. Degradation of azo dye Procion Red MX-5B by photocatalytic oxidation. *Chemosphere* **46**:905-912; 2002.
- [71] Guillard, C.; Lachheb, H.; Houas, A.; Ksibi, M.; Elaloui, E.; Herrmann, J. M. Influence of chemical structure of dyes, of pH and of inorganic salts on their photocatalytic degradation by TiO₂ comparison of the efficiency of powder and supported TiO₂. *Journal of Photochemistry and Photobiology a-Chemistry* **158**:27-36; 2003.
- [72] Sun, B.; Smirniotis, P. G. Interaction of anatase and rutile TiO₂ particles in aqueous photooxidation. *Catalysis Today* **88**:49-59; 2003.
- [73] Houas, A.; Lachheb, H.; Ksibi, M.; Elaloui, E.; Guillard, C.; Herrmann, J. M. Photocatalytic degradation pathway of methylene blue in water. *Applied Catalysis B-Environmental* **31**:145-157; 2001.
- [74] Konstantinou, I. K.; Albanis, T. A. TiO₂-assisted photocatalytic degradation of azo dyes in aqueous solution: kinetic and mechanistic investigations - A review. *Applied Catalysis B-Environmental* **49**:1-14; 2004.

BIOGRAPHICAL SKETCH

Rui Qing was born in Hanshan, a small town in Anhui, China in 1985. He moved to Hefei, the capital of Anhui province after 2 years elementary education in his hometown. Having attended the entrance examination for higher education in China, he was admitted in 2003 by Tongji University, Shanghai, China, majoring in materials science and engineering. He received his bachelor's degree in science in June 2007 after 4 years undergraduate study. He then sought for a further education overseas and joined the Department of Materials Science and Engineering in University of Florida from August 2007. Up until now he has been working in Dr. Sigmund's group and expecting to receive his master's degree in May 2009.

In the undergraduate education in Tongji University, Rui specialized in non-metallic, inorganic materials. He had worked on a project aimed to investigate the glass forming region of telluride-niobium-phosphate ternary glass system and their properties. These materials could potentially be used as lenses material in digital camera and optical microscopy. He was also awarded 3rd rank scholarship for excellent students in Tongji University for academic year 2003-2004 and 2004-2005.

In his master's study under Dr. Sigmund's supervision, Rui advanced the understanding of photocatalytic activity of cerium-zirconium dioxide solid solution nanoparticles. Widely used as three catalyst in automobiles and electrolyte materials in solid oxide fuel cells, cerium-zirconium dioxide solid solutions were investigated for their free radical scavenging property in biomedical uses. However, as a semiconductor these materials might be able to generate ROS (Reactive Oxygen Species) though they are capable of scavenging them. In the project Rui and his advisor successfully proved the photocatalysis of cerium-zirconium dioxide nanoparticles and compare them to the commercialized photocatalyst. They are also preparing a paper for publication from the results achieve